3. Generation and Propagation of G Waves from the Niigata Earthquake of June 16, 1964.

Part 1. A statistical analysis.

By Keiiti AKI,

Earthquake Research Institute.

Summary

The G waves from the Niigata earthquake of June 16, 1964 recorded at the world-wide standard seismograph stations are studied for the purpose of elucidating the source mechanism.

The observed radiation pattern of $G2$ waves with period 200 sec indicates a source of pure thrust fault with the strike direction N20°E. This result is in excellent agreement with those from the first motion study as well as from the field studies of the epicentral area by various geological and geophysical methods.

The amplitude and phase spectra for shorter periods are variable, and a statistical approach is taken in their investigation. Both $G2$ and $G3$ waves with periods shorter than about 150 sec show a statistical behavior expected for a finite sample of a smoothed Gaussian noise. The factors causing this randomization may be 1) the source complex, 2) the interference due to lateral refraction, and 3) the interference with higher modes or body waves.

The near-pole phenomena are demonstrated on a before-after picture by the forward extrapolation of $G2$ wave fronts and the backward extrapolation of $G3$ wave fronts. It is confirmed that the $\pi/2$ polar phase advance is a good first approximation. However, the "after" picture obtained from $G3$ waves shows much greater irregularity than the "before" picture obtained from $G2$ waves, and it is difficult to find the source mechanism by the phase equalization of $G3$ waves.

The apparent Q values estimated from averaged spectra vary from 100 to 200 for the periods from 200 to 50 sec.

§1. Introduction.

The world-wide standard seismographs ($WWSS$) distributed by the Coast and Geodetic Survey now furnish the seismologist with data

appropriate for investigating the generation and propagation of seismic waves on an absolutely quantitative basis. In the present paper, we studied the G waves generated by the Niigata earthquake $(M=7.5)$ of June 16, 1964.

The phase and amplitude equalization method of determining the source parameters developed in recent years[1) to 21)] will be successfully applied to the G waves with period of 200 sec. The applicability of the method to shorter period waves will be investigated by a statistical analysis of the variability of phase and amplitude spectra.

From the G wave amplitude spectral density we shall, in Part 2 of this paper, estimate the magnitude of moment of component couple of the double couple assumed as the source model. Using the dynamical equivalence relation between the double couple and a slip dislocation, we shall estimate the amount of dislocation, and further the energy released by such dislocation and the stress-strain drop which occurred at the source of this earthquake.

The Niigata earthquake offers an excellent case for such an investigation, because we are given a picture of crustal deformation accompanied by the earthquake from detailed field studies. This earthquake may be

1) J. N. Brune, J. E. Nafe and J. Oliver, *J. Geophys. Res.*, **65** (1960), 287-304.

2) K. Aki, *J. Goephys. Res.*, **65** (1960), 323-331.

3) K. Aki, *J. Geophys. Res.*, **65** (1960), 729-740.

4) K. Aki, *J. Geophys. Res.*, **65** (1960), 2405-2417.

5) K. Aki, *J. Geophys. Res.*, **65** (1960), 4165-4172.

6) J. N. Brune, *Publ. Dominion Obs.*, **26** (1961), No. 10.

7) J. N. Brune, J. E. Nafe and L. E. Alsop, *Bull. Seis. Soc. Amer.*, **51** (1961), 247-258.

8) J. N. Brune, H. Benioff and M. Ewing, *J. Geophys. Res.*, **66** (1961), 2895-2910.

9) F. Press, A. Ben-Menaham and M. N. Toksöz, *J. Geophys. Res.*, **66** (1961), 3471-3485.

10) K. Aki, *Bull. Earthq. Res. Inst.*, **40** (1962), 91-105.

11) K. Aki, *J. Geophys. Res.*, **67** (1962), 3645-3647.

12) A. Ben-Menahem and M. N. Toksöz, *J. Geophys. Res.*, **67** (1962), 1943-1955.

13) A. Ben-Menahem and M. N. Toksöz, *J. Geophys. Res.*, **68** (1963), 5207-5222.

14) A. Ben-Menahem and M. N. Toksöz, *Bull. Seis. Soc. Amer.*, **53** (1963), 905 920.

15) S. W. Smith, *J. Geophys. Res.*, **68** (1963), 1477-1483.

16) J. N. Brune and P. W. Pomroy, *J. Geophys. Res.*, **68** (1963), 5005-5028.

17) K. Aki, *Bull. Seis. Soc. Amer.*, **54** (1964), 511-570.

18) K. Aki, *J. Geophys. Res.*, **69** (1964), 1131 1134.

19) M. N. Toksöz and A. Ben-Menahem, *J. Geophys. Res.*, **69** (1964), 1639-1648.

20) M. N. Toksöz, A. Ben-Menahem and D. G. Harkrider, *J. Geophys. Res.*, **69** (1964), 4355-4366.

21) M. N. Toksöz, D. G. Harkrider and A. Ben-Menahem, *J. Geophys. Res.*, **70** (1965), 907-922.

like a controlled experiment, in which we can check the applicability of the surface wave method of source study and consequently the fundamental assumptions underlying the method. Our result strongly supports one such assumption that the earthquake is a release of accumulated strain energy by a rupture.

The field study of this earthquake has been made by all available geological and geophysical methods. It is found[22),23)] that the aftershock area is a strip trending roughly N20°E with length about 100 km and width about 30 km. Most of the aftershocks are located at depths shallower than 25 km. The source area of tsunami generated by this earthquake approximately coincides with the aftershock area.[24)] The epicentre of the main shock is not located at an end of the aftershock area but situated near the centre slightly departing toward south-west. The focal depth of the main shock is reported as 40 km by the Japan Meteorological Agency (*JMA*). As shown later, a recomputation based on revised crust-mantle models gives the depth of 10 to 20 km. The aftershock area lies between Honshu and a small island called Awashima. At the time of the earthquake, this island was upheaved by about 1.5 m,[25)] while the coast of Honshu subsided by 0.1 to 0.3 m.[26),27)] The upheaval in Awashima is greater on its east side than on the west, indicating a tilting of about 1 minute.[28)] The direction of the largest tilt is perpendicular to the general trend of the island, which coincides with the trend of the aftershock belt mentioned above. Several submarine faults are found by the echo-sounding[29)] and sparker method.[30)] They trend again roughly N20°–30°E. The maximum upheaval and subsidence of the ocean bottom during the earthquake found by the echo-sounding is 6 and 4 meters respectively.

22) Technical report of Japan Meteorological Agency, No. 43, 1965.

23) I. KAYANO, reported at the meeting of the Seismological Society of Japan, Oct., 1965.

24) I. AIDA, K. KAJIURA, T. HATORI and T. MOMOI, *Preliminary Reports on the Niigata Earthquake of June* 16, 1964 (*Spec. Bull. Earthq. Res. Inst.*, **8**, 1964), 58–62.

25) K. NAKAMURA, K. KASAHARA and T. MATSUDA, *Jour. Geod. Soc. Japan*, **10** (1964), 172–179.

26) I. TSUBOKAWA, Y. OGAWA and T. HAYASHI, *Jour. Geod. Soc. Japan*, **10** (1964), 165–171.

27) K. MOGI, *Preliminary Reports on the Niigata Earthquake of June* 16, 1964 (*Spec. Bull. Earthq. Res. Inst.*, **8**, 1964), 46–51.

28) K. NAKAMURA *et al.* loc. cit., 25).

29) A. MOGI, B. KAWAMURA and Y. IWABUCHI, *Jour. Geod. Soc. Japan*, **10** (1964), 180–186.

30) M. HAYAKAWA *et al.* reported at the meeting of the Seismological Society of Japan, May, 1965.

To sum up, the field studies suggest that the source of the Niigata earthquake may be a bilateral faulting extending about 100 km in total with the strike direction N20°–30°E and the vertical off-set of several meters, north-west side being upheaved.   It will be shown that this picture of the source mechanism is in excellent harmony with observations on body and surface waves generated from this earthquake.

§ 2.   Data.

We have collected through the Coast and Geodetic Survey full sized copies of long and short period seismograph records of the Niigata earthquake obtained at the world-wide standard stations.   Table 1 shows the
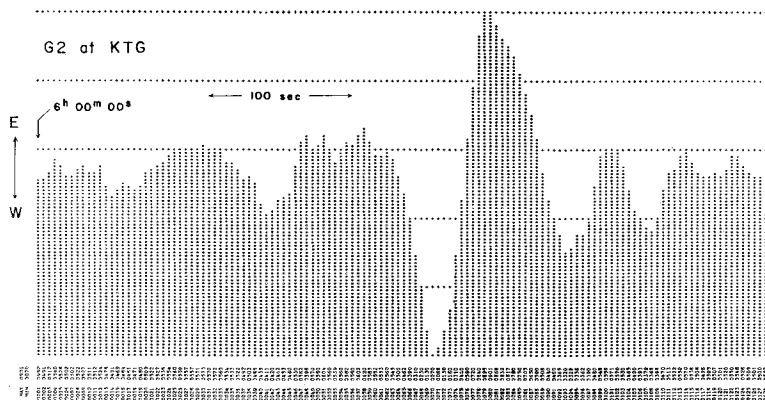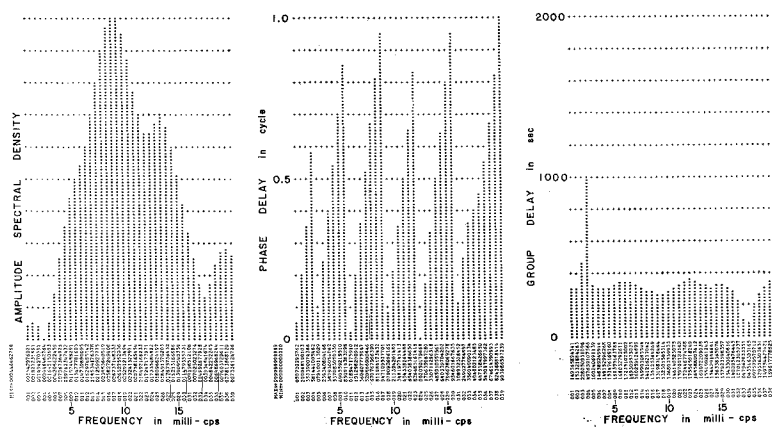

Fig. 1   Computer plot of a typical G wave form.

Fig. 2   Amplitude spectral density, phase delay and group delay for the wave form shown in Fig. 1.

Table 1. List of stations

No.	Station	Latitude deg. min. sec.			Longitude deg. min. sec.			First motion	Epicentral distance (km)	Azimuth at epicentre (deg)	Azimuth at station (deg)	Half great circle (km)
1	MTJ	36	12	39.0 N	140	6	36.0 E	D	253.8	161.5	-17.9	20006.6
2	SEO	37	34	0. N	126	58	0. E		1079.4	-91.0	81.4	20025.1
3	ANP	25	11	0. N	121	31	0. E	C?	2218.1	-126.1	44.4	20018.0
4	GUA	13	35	18.0 N	144	54	42.0 E	C	2804.3	166.9	-10.5	20005.6
5	HKC	22	18	12.8 N	114	10	18.8 E	D?	2979.2	-119.5	47.6	20020.1
6	BAG	16	24	39.0 N	120	34	47.0 E	C	3040.5	-138.1	33.1	20013.7
7	MAN	14	40	0. N	121	5	0. E		3175.7	-140.9	30.8	20012.7
8	NHA	12	12	36.0 N	109	12	42.0 E	C	4151.2	-126.2	40.4	20018.0
9	CHG	18	47	24.0 N	98	58	37.0 E	D?	4446.6	-107.7	52.2	20023.2
10	RAB	4	11	33.0 S	152	10	16.0 E	C	4899.5	161.2	-14.7	20006.7
11	SHL	25	34	0. N	91	53	0. E	D?	4639.0	-93.5	60.2	20025.1
12	PMG	9	24	33.0 S	147	9	14.0 E	C?	5354.5	169.4	-8.4	20005.3
13	HNR	9	25	53.9 S	159	56	47.6 E	C	5714.4	153.4	-20.9	20008.7
14	HOW	22	25	0. N	88	18	33.0 E		5130.5	94.9	57.7	20025.0
15	COL	64	54	0. N	147	47	36.0 W	C	5431.8	32.7	85.7	20010.6
16	NDI	28	41	0. N	77	13	0. E	D?	5751.5	81.1	62.0	20024.7
17	HON	21	19	18.0 N	158	0	30.0 W	C	6231.4	88.5	-57.4	20025.1
18	KIP	21	25	24.0 N	158	0	54.0 W	C	6224.8	88.4	-57.4	20025.1
19	LAH	31	33	0. N	74	20	0. E		5853.1	76.4	63.5	20024.0
20	AFI	13	54	33.6 S	171	46	38.1 W	C	7715.7	128.3	-39.4	20017.2
21	CTA	20	5	18.0 S	146	15	16.0 E	D?	6514.0	172.2	-6.5	20005.0
22	QUE	30	11	0. N	66	57	0. E	C?	6547.9	-74.3	60.9	20023.6
23	NOR	81	36	0. N	16	41	0. E		6616.4	4.0	21.8	20004.7
24	SUV	18	8	56.0 S	178	27	26.0 E	C	7479.5	139.2	-32.7	20013.3
25	KEV	69	45	24.0 N	27	0	54.0 E		6835.1	21.5	55.8	20007.3
26	CMC	67	50	12.0 N	115	5	0. W		6726.0	24.8	-60.2	20008.2
27	RES	74	41	0. N	94	54	0. W		6853.5	14.1	-46.3	20005.8
28	CCG	77	10	0. N	61	8	0. E	C	7108.2	5.0	17.7	20004.7
29	ADE	34	58	1.0 S	138	42	32.0 E		8121.3	-179.6	0.4	20004.6
30	PER	31	57	9.6 S	115	50	22.0 E	C	8155.2	-159.3	19.0	20007.1
31	MUN	31	58	30.0 S	116	12	24.0 E	C	8146.4	-159.6	18.8	20007.1
32	RIV	33	49	45.7 S	151	9	30.0 E		8089.7	169.6	-9.8	20005.2
33	LON	46	45	0. N	121	48	36.0 W	C	7623.1	46.7	-56.4	20015.5
34	COR	44	35	8.6 N	123		11.5 W	C	7659.1	49.3	-56.5	20016.4
35	UME	63	48	54.0 N	20	14	12.0 E		7478.0	24.8	48.1	20008.2

(to be continued)

Table 1. (continued)

No.	Station	Latitude deg. min. sec.	Longitude deg. min. sec.	First motion	Epicentral distance (km)	Azimuth at epicentre (deg)	Azimuth at station (deg)	Half great circle (km)
36	NUR	60 30 32.2 N	24 39 18.1 E	C	7544.1	− 29.0	50.4	20009.4
37	SHI	29 30 40.0 N	52 31 34.0 E	D?	7778.2	− 67.7	56.5	20022.2
38	UPP	59 51 29.0 N	17 37 37.0 E		7881.2	− 27.0	45.0	20008.8
39	KON	59 40 0. N	9 40 0. E	C	8196.3	− 24.0	39.0	20008.0
40	KTG	70 25 0. N	21 58 0. E	C	7843.7	− 6.6	15.6	20004.8
41	GDH	69 15 0. N	53 32 0. W	C	8023.0	4.7	− 10.5	20004.7
42	TAU	42 54 35.7 S	147 19 13.5 E	C	9040.1	174.0	− 6.5	20004.8
43	BKS	37 52 36.0 N	122 14 6.0 W	C	8157.6	54.6	− 54.1	20018.2
44	BOZ	45 36 0. N	111 38 0. W	C	8328.7	43.3	− 50.1	20014.2
45	COP	55 41 0. N	12 26 0. E	C	8432.2	− 27.8	40.4	20009.0
46	PAS	34 8 54.0 N	118 10 18.0 W	C	8699.5	55.6	− 51.4	20018.6
47	GSC	35 6 59.5 N	116 48 16.6 W		8729.9	54.1	− 51.0	20018.1
48	DUG	40 11 42.0 N	112 48 48.0 W	C	8641.6	48.1	− 49.8	20016.0
49	IST	41 2 36.0 N	28 59 6.0 E	C	8725.0	46.3	48.7	20015.3
50	ESK	55 19 0. N	3 12 0. W		9026.8	20.6	28.9	20007.1
51	RCD	44 4 30.0 N	103 12 30.0 W		8933.9	40.3	− 44.8	20013.2
52	WEL	41 17 12.0 S	174 46 0. E	C	9532.8	153.9	− 27.4	20008.6
53	GOL	39 42 1.0 N	105 22 16.0 W	C	9148.8	44.6	− 45.6	20014.7
54	TUC	32 18 35.0 N	110 46 56.0 W	C	9356.1	53.0	− 47.8	20017.7
55	ALQ	34 56 30.0 N	106 27 30.0 W	C	9448.8	48.6	− 45.8	20016.1
56	MNN	44 54 52.0 N	93 11 24.0 W	C	9394.7	34.3	− 38.6	20011.1
57	VAL	51 56 0. N	10 15 0. W	C	9570.1	− 18.3	23.5	20006.6
58	STU	48 46 15.0 N	9 16 36.0 E		9166.7	− 30.7	37.3	20009.9
59	TRI	45 42 32.0 N	13 45 51.0 E		9220.0	− 35.0	40.1	20011.3
60	ATU	37 58 22.0 N	23 43 0. E		9288.7	− 45.8	45.4	20015.1
61	ATH	37 58 20.0 N	23 43 0. E	C	9288.7	− 45.8	45.4	20015.1
62	HLW	29 51 30.0 N	31 20 30.0 E		9386.1	− 56.0	48.6	20018.7
63	AQU	42 21 14.0 N	13 24 11.0 E		9524.9	− 37.0	39.6	20012.0
64	LUB	33 35 0. N	101 52 0. W		9852.8	46.8	− 43.4	20015.5
65	MDS	43 22 20.0 N	89 45 36.0 W		9697.5	33.3	− 36.3	20010.8
66	FLO	38 48 6.0 N	90 22 12.0 W	C	10075.5	36.4	− 36.6	20011.8
67	AAM	42 17 59.0 N	83 39 22.0 W	C	10076.7	30.2	− 32.2	20009.8
68	DAL	32 50 46.0 N	96 47 2.0 W		10230.3	44.2	− 40.6	20014.5
69	OXF	34 30 52.0 N	89 24 39.0 W		10509.5	38.3	− 36.2	20012.5
70	SHA	30 41 41.1 N	88 8 23.0 W	C	10922.7	39.7	− 35.6	20012.9

Table 1. (continued)

No.	Station	Latitude deg. min. sec.				Longitude deg. min. sec.				First motion	Epicentral distance (km)	Azimuth at epicentre (deg)	Azimuth at station (deg)	Half great circle (km)
71	ATL	33	26	0.0	N	84	20	15.0	W	C	10874.1	35.4	—33.0	20011.5
72	BLA	37	12	40.0	N	80	25	14.0	W	C	10703.6	30.7	—30.2	20009.9
73	SCP	40	48	35.5	N	77	52	9.8	W	C	10462.6	27.2	—28.3	20008.9
74	OGD	41	4	0.	N	74	37	0.	W	C	10562.0	24.9	—26.0	20008.2
75	GEO	38	54	0.	N	77	4	31.0	W	C	10682.1	27.6	—27.8	20009.0
76	PAL	41	0	25.0	N	73	54	19.5	W	C	10593.8	24.5	—25.5	20008.1
77	WES	42	23	4.9	N	71	19	6.0	W		10543.8	22.1	—23.5	20007.5
78	PTO	41	8	12.0	N	8	36	55.0	W		10614.4	23.8	—24.8	20007.9
79	TOL	39	52	53.0	N	4	2	40.0	W	C	10567.6	27.4	—28.1	20008.9
80	MAL	36	43	39.0	N	4	24	56.0	W	C	10891.7	28.7	—28.0	20009.3
81	AAE	9	1	0.	N	38	45	13.2	E		10293.0	76.3	—50.6	20024.0
82	NAI	1	16	26.2	S	36	48	0.	E	C	11182.2	83.0	—51.3	20024.8
83	HLL	72	18	50.0	N	170	13	0.	W	C	12512.2	170.1	—26.1	20005.2
84	LWI	2	15	0.	S	28	48	42.0	E		11940.7	78.6	—50.5	20024.3
85	PDA	37	44	36.0	N	25	39	52.0	W		11434.8	12.2	—12.1	20005.5
86	BEC	32	22	46.0	N	64	40	43.0	W		11791.1	20.8	—19.3	20007.2
87	LPS	14	17	32.0	N	89	9	0.	W		12311.3	50.6	—38.8	20016.8
88	SBA	77	51	0.	S	166	46	48.0	E		13029.8	173.6	—24.2	20004.8
89	BUL	20	8	36.0	S	28	36	0.	E		13144.8	93.9	—56.7	20025.0
90	PRE	25	45	0.	S	28	15	0.	E		13506.9	99.1	—59.5	20024.6
91	BHP	8	57	39.0	N	79	33	29.0	W		13409.7	45.7	—34.8	20015.1
92	SPA	90	0	0.	S	0	0	39.5	E		14252.4	—180.0	139.2	20004.6
93	CAR	10	30	24.0	N	66	55	54.0	W		13954.2	32.0	—25.1	20010.3
94	BOG	4	37	23.0	N	74	3	1.8	W		14145.3	43.2	—32.8	20014.2
95	QUI	0	12	0.5	S	78	30	0.	W		14297.5	51.2	—38.0	20017.1
96	WIN	22	34	0.	S	17	6	6.0	E		14294.9	89.3	—58.5	20025.1
97	TRN	10	18	0.	N	61	24	30.0	W		14172.3	25.7	—20.4	20008.4
98	SNA	70	19	32.0	S	2	21	31.7	W		15811.4	—159.7	127.4	20007.0
99	NNA	11	59	15.2	S	76	50	28.6	W		15406.4	60.0	—44.5	20020.0
100	ARE	16	27	43.5	S	71	29	54.1	W		16163.9	59.0	—45.1	20019.7
101	LPB	16	31	57.6	S	68	5	54.0	W		16418.1	54.8	—42.6	20018.3
102	ANT	23	41	56.0	S	70	24	7.0	W		16780.2	67.8	—53.3	20022.2
103	PEL	33	8	37.0	S	70	41	52.0	W		17272.2	86.1	—70.1	20025.1
104	LPA	34	54	32.0	S	57	55	24.0	W		18446.5	79.6	—72.3	20024.5
105	RDJ	22	53	42.0	S	43	13	12.0	W		18272.2	8.2	—7.3	20005.0
106	CMO	64	51	36.0	N	147	50	0.	W		5430.1	32.8	—85.7	20010.6

epicentral distance and azimuth to each station from the epicentre, together with the azimuth to the epicentre at the station and one half of the length of complete great circle path through the station. The epicentre coordinates are taken as 38°23'N and 139°13'E, and computation is made by the use of the Rudoe's formula.

In the present paper, only those records are used which show well isolated G waves with amplitudes significantly above the background noise. G waves are identified by the arrival time and polarization, their record amplitudes digitized to one-tenth of a mm at 4 sec intervals by a manual method and punched on a paper tape. The error in digitizing is checked by comparing the original record with the computer plot (Fig. 1) of the digital data. Then, the amplitude spectral density $|F(\omega)|$, phase delay $\phi(\omega)$ and group delay $\dfrac{d\phi}{d\omega}$ are computed (Fig. 2). These are defined by

$$f(t) = \frac{1}{\pi} \int_0^\infty |F(\omega)| \cos(\omega t - \phi(\omega)) d\omega \ , \tag{1}$$

where $f(t)$ is the G wave record, t being measured from the time of the first data point. No smooth window is used in computing the spectra, because most of the records chosen for Fourier analysis show well isolated wavelets, and the window is practically unnecessary. The average time length of one record is 519 sec for $G2$ waves, 537 sec for $G3$ and 593 sec for $G4$.

Table 2 shows the amplitude spectral density $|F(\omega)|$ in unit of cm sec. These values refer to the record trace, and not to the true ground displacement. In order to see the effect to noise or error in measurement on the tabulated values, we made the following error estimation.

Let S_i and N_i be the ith sample values of the signal and the Gaussian noise with the RMS amplitude of σ respectively, then the cosine term $a_j = \varDelta t \sum_i (S_i + N_i) \cos 2\pi \dfrac{ij\varDelta t}{T_0}$ will follow the Gaussian distribution with the mean value

$$\bar{a}_j = \varDelta t \sum_i S_i \cos 2\pi \frac{ij\varDelta t}{T_0} \ , \tag{2}$$

and the variance

$$\overline{\{a_j - \bar{a}_j\}^2} = \frac{T_0 \cdot \varDelta t}{2} \sigma^2. \tag{3}$$

Table 2. List of amplitude spectral density

(unit in cm sec on the record, without instrumental correction)

Station	Wave type	Component Magnification	Frequency in c/s										
			.0050	.0065	.0080	.0095	.0110	.0125	.0140	.0155	.0170	.0185	.0200
GDH	G2	EW, 750	50	93	138	157	145	160	156	133	163	182	103
GDH	G3	EW, 750	25	38	51	48	53	24	22	21	17	15	12
GDH	G4	EW, 750	22	23	29	24	9	2	9	3	4	1	2
OGD	G3	EW, 3000	87	117	169	185	123	57	52	72	55	8	2
OGD	G4	EW, 3000	43	65	43	75	65	40	22	10	19	35	29
TRN	G2	EW, 750	48	88	167	223	258	287	297	346	317	147	33
TRN	G3	EW, 750	13	29	35	15	14	4	11	28	9	14	4
TRN	G4	EW, 750	36	45	34	33	37	12	15	32	9	2	7
CAR	G3	EW, 3000	41	139	138	103	51	35	140	69	86	64	29
CAR	G4	EW, 3000	88	55	101	124	134	65	49	30	17	16	8
COL	G3	NS, 1500	109	156	167	163	133	77	71	75	47	6	25
COL	G5	NS, 1500	42	39	19	14	15	5	6	6	4	3	2
GOL	G2	EW, 1500	61	75	49	83	42	188	214	133	116	107	41
GOL	G3	EW, 1500	111	192	219	210	88	15	57	28	5	5	13
BHP	G2	EW, 750	65	68	33	66	148	141	172	165	29	81	44
BHP	G3	EW, 750	33	41	41	26	30	36	20	6	3	5	4
LON	G3	NS, 1500	92	94	81	73	42	44	28	25	26	34	18
COR	G3	NS, 1500	98	71	75	58	64	67	24	26	44	22	9
QUI	G3	EW, 1500	125	153	128	104	103	76	20	41	16	4	19
LPS	G2	EW, 750	47	106	162	78	150	185	120	123	156	89	32
LPS	G3	EW, 750	65	78	69	61	54	30	11	29	19	4	7
TUC	G2	NS, 1500	179	235	184	192	290	116	46	181	73	54	105
TUC	G3	NS, 1500	85	84	92	116	105	68	150	42	38	15	3
GSC	G2	NS, 1500	48	49	80	96	40	40	52	52	76	57	15
GSC	G3	NS, 1500	14	18	27	4	23	11	15	11	15	12	5
LPB	G3	EW, 1500	136	110	52	72	72	76	82	62	22	13	15
ARE	G3	EW, 1500	115	95	69	78	76	154	60	63	25	15	39
PEL	G3	NS, 1500	115	20	88	44	66	64	26	12	29	12	1
KIP	G3	NS, 1500	92	115	63	58	108	115	86	62	32	31	17
AFI	G3	EW, 750	29	33	20	7	57	53	3	23	7	19	15
HNR	G2	EW, 750	61	90	146	224	179	97	175	131	62	235	17

(to be continued)

Table 2. (continued)

Station	Wave type	Component Magnification	Frequency in c/s										
			.0050	.0065	.0080	.0095	.0110	.0125	.0140	.0155	.0170	.0185	.0200
HNR	G3	EW, 750	62	111	69	73	94	50	30	18	51	24	29
HNR	G4	EW, 750	14	27	17	7	20	21	8	7	4	1	4
RAB	G3	EW, 750	348	290	212	130	63	39	61	95	93	57	37
GUA	G2	EW, 750	113	192	172	112	111	136	133	86	38	62	46
GUA	G3	EW, 750	45	38	33	57	73	63	70	76	62	38	19
TAU	G2	EW, 750	60	90	68	60	47	102	30	37	88	47	45
TAU	G3	EW, 750	40	42	32	25	15	25	12	19	24	35	2
ADE	G2	EW, 750	62	20	59	170	175	43	91	139	19	27	70
ADE	G3	EW, 750	38	31	22	15	29	43	45	20	0	17	16
BAG	G3	EW, 1500	118	135	238	347	371	262	78	85	109	42	78
BAG	G4	EW, 1500	6	54	40	26	46	35	10	6	8	9	10
BAG	G5	EW, 1500	36	36	52	58	35	27	18	13	4	9	4
NHA	G2	EW, 1500	229	297	281	404	401	176	172	169	17	98	98
NHA	G4	EW, 1500	49	43	24	7	17	20	15	13	4	6	7
HKC	G2	EW, 750	76	121	124	99	73	41	31	24	24	35	22
SHI	G3	NS, 1500	45	53	126	39	108	36	60	73	33	60	55
COP	G2	EW, 375	40	51	27	26	31	26	38	12	26	43	28
COP	G3	EW, 375	18	20	37	26	26	33	11	20	6	8	12
KON	G3	EW, 1500	115	69	73	135	84	87	59	55	99	51	37
PTO	G2	EW, 750	101	103	72	85	158	214	247	239	155	46	29
PTO	G4	EW, 750	42	39	41	20	42	69	72	33	16	7	16
ESK	G2	EW, 1500	24	28	16	4	17	10	15	10	4	7	3
ESK	G3	EW, 1500	139	179	139	47	153	262	277	135	228	204	69
VAL	G2	EW, 750	86	93	114	61	15	138	89	50	32	33	23
VAL	G3	EW, 750	74	89	131	103	32	11	72	97	63	39	43
VAL	G4	EW, 750	22	20	47	32	34	47	56	32	24	16	15
KTG	G2	EW, 750	25	20	11	18	8	6	8	6	4	4	1
KTG	G4	EW, 750	119	163	239	265	208	173	179	115	50	65	73
NOR	G2	EW, 810	43	51	45	31	23	25	42	36	28	7	8
NOR	G3	EW, 810	33	41	18	12	13	10	12	4	4	1	3

The sine term b_j will follow the same distribution with the same variance as a_j. Thus,

$$[\{a_j - \bar{a}_j\}^2 + \{b_j - \bar{b}_j\}^2] \Big/ \frac{T_0 \cdot \Delta t}{2} \sigma^2$$

will follow the χ^2 distribution with two degrees of freedom. Then, the average value of $A = [\{a_j - \bar{a}_j\}^2 + \{b_j - \bar{b}_j\}^2]^{1/2}$ may be expressed as

$$\bar{A} = \int_0^\infty \frac{2A^2}{T_0 \cdot \Delta t \cdot \sigma^2} \exp\left(\frac{-A^2}{T_0 \cdot \Delta t \cdot \sigma^2}\right) dA = \sqrt{\frac{\pi}{2}} \cdot \sqrt{\frac{T_0 \cdot \Delta t}{2}} \cdot \sigma. \tag{4}$$

In the absence of the signal $(\bar{a}_j = \bar{b}_j = 0)$, average amplitude spectral density of the noise may be estimated by use of the above formula, if the record length T_0, sample interval Δt and σ are given. If the *RMS* noise amplitude is 1 mm on the record, the density for the sample length corresponding to $G2$ waves will be around 4.0 cm sec. For $G3$ and $G4$, they will be 4.1 and 4.3 cm sec respectively. In using the data in Table 2, we must be cautious with the use of values comparable or smaller than the above noise level. In the presence of the signal, the contribution from noises to the power spectrum may be estimated by the following formula,

$$\overline{a_j^2 + b_j^2} = \bar{a}_j^2 + \bar{b}_j^2 + \overline{A^2} \tag{5}$$

where, $\overline{A^2} = T_0 \cdot \Delta t \cdot \sigma^2$ is the average contribution from noises.

We must note here that except for reading errors, the actual noises are not statistically independent between the consecutive sample points, but show smooth long period oscillations on the record. This kind of noise may be roughly expressed as a moving average of the Gaussian noise. The *RMS* amplitude of such noises will be $1/\sqrt{n}$ of that of the original Gaussian noise, where n is the number of points over which the average is taken. For such cases, the noise spectral density of 4.0 cm sec for $G2$ waves would not correspond to the noise level of 1 mm observed on the record but to that of $1/\sqrt{n}$ mm.

Table 3 shows the phase delay time, $(t_1 - t_0) + \phi(\omega)/\omega$, where t_1 is the time of the first data point and t_0 is the origin time of the earthquake $(4^h 01^m 41^{sec}, GCT)$. The values are uncertain by integer multiples of period T. The phase delay time in Table 3 refers to the peak of transverse motion on the record in the counterclockwise direction as seen from the epicentre. The values are not yet corrected for instrumental phase shift.

Table 3. List of phase delay time

(travel time of the peak of counterclockwise motion, without instrumental correction)

(uncertain by integer multiples of period T)

Station	Wave type	$f = .005$ c/s $T = 200$ sec	.0065 153.8	.008 125.0	.0095 105.3	.0110 90.9	.0125 80.0
GDH	G2	7147 sec	7165 sec	7189 sec	7203 sec	7217 sec	7221 sec
GDH	G3	10851	10858	10879	10891	10902	10908
GDH	G4	15921	16019	16078	16098	16096	16130
OGD	G3	11457	11461	11467	11477	11488	11503
OGD	G4	15527	15565	15587	15599	15631	15664
TRN	G2	5823	5838	5840	5840	5843	5850
TRN	G3	12183	12190	12217	12209	12224	12275
TRN	G4	14849	14856	14864	14875	14891	14923
CAR	G3	12139	12173	12192	12211	12228	12257
CAR	G4	14841	14850	14857	14883	14887	14896
COL	G3	10285	10327	10352	10368	10382	10466
COL	G5	19365	19424	19473	19502	19506	19515
GOL	G2	6881	6936	7017	7024	7000	6998
GOL	G3	11271	11293	11305	11310	11319	11321
BHP	G2	6015	6038	6033	6058	6063	6066
BHP	G3	12323	12319	12314	12309	12297	12301
LON	G3	10969	10976	10976	10970	10962	10950
COR	G3	10979	10984	10973	10972	10960	10963
QUI	G3	12519	12515	12514	12514	12516	12516
LPS	G2	6239	6281	6298	6320	6354	6361
LPS	G3	11917	11950	11977	11997	12009	12017
TUC	G2	6853	6910	6935	6971	6983	6984
TUC	G3	11125	11179	11218	11234	11219	11233
GSC	G2	7169	7196	7209	7209	7213	7250
GSC	G3	11011	11038	11054	11081	11116	11097
LPB	G3	12737	12790	12800	12826	12853	12897
ARE	C3	12695	12761	12807	12840	12859	12863
PEL	G3	12863	12861	12919	12964	12950	12951
KIP	G3	10437	10451	10473	10482	10472	10470
AFI	G3	10617	10684	10704	10749	10763	10772
HNR	G2	7633	7667	7700	7726	7739	7759

Table 3. (continued)

Station	Wave type	$f=.005$ c/s $T=200$ sec	.0065 153.8	.008 125.0	.0095 105.3	.0110 90.9	.0125 80.0
HNR	G3	10199 sec	10259 sec	10287 sec	10302 sec	10294 sec	10294 sec
HNR	G4	16835	16862	16872	16880	16878	16879
RAB	G3	10257	10266	10271	10277	10288	10302
GUA	G2	8433	8453	8465	8468	8475	8489
GUA	G3	9841	9887	9883	9854	9855	9857
TAU	G2	6991	7015	7031	7053	7046	7043
TAU	G3	11815	11321	11317	11321	11309	11298
ADE	G2	7157	7196	7293	7299	7297	7294
ADE	G3	10897	10938	10964	10980	11006	11022
BAG	G3	9543	9564	9588	9611	9628	9639
BAG	G4	17433	17454	17479	17482	17506	17525
BAG	G5	18545	18590	18612	18632	18671	18701
NHA	G2	8091	9924	9953	9968	9975	9974
NHA	G4	17137	17211	17235	17273	17278	17288
HKC	G2	8521	8530	8537	8539	8542	8553
SHI	G3	10863	10922	10950	10958	10977	10994
COP	G2	7097	7132	7150	7150	7162	7159
COP	G3	10953	10953	10966	10982	10994	11006
KON	G3	10896	10920	10936	10940	10943	10950
PTO	G2	6657	6675	6687	6682	6682	6684
PTO	G3	11385	11414	11438	11455	11457	11473
PTO	G4	15679	15702	15705	15689	15672	15678
ESK	G2	6983	7015	7028	7013	7030	7033
ESK	G3	10819	10931	10994	11034	11036	11037
VAL	G2	6875	6905	6917	6914	6902	6862
VAL	G3	11193	11211	11237	11263	11297	11304
VAL	G4	15903	15948	15962	15977	15996	15970
KTG	G2	7239	7282	7308	7317	7326	7339
KTG	G3	10883	10916	10928	10930	10907	10906
KTG	G4	16471	16507	16515	16519	16521	16525
NOR	G2	7469	7515	7525	7518	7536	7572
NOR	G3	10319	10496	10528	10582	10569	10575

The sense of the first motion at each station has been read by Hirasawa[31] directly from the seismogram and is included in Table 1.

Tables 1 to 3 include all the data on which the analyses in the following chapters are applied.

§ 3. Radiation pattern of G2 waves with period of 200 sec.

The wave length of G waves corresponding to period of 200 sec is about 1,000 km.   Since the linear dimension of the source of the Niigata earthquake seems not to exceed 100 km as the aftershock area and the Tsunami source area indicate, we may safely assume that the source is a point for the wave with period of 200 sec.

For the first approximation, we shall further assume that the source is a double couple operated in the form of a step function in time.   Under these assumptions, we may find the orientation of the double couple or the mode of fault motion by comparing theoretical and observed phase and amplitude spectra at various azimuths from the epicentre.   In order to do this, we must first correct the observed spectra for propagation and recording.

The correction required for the observed phase of G waves may be expressed by the following formula.

$$\phi_s = \frac{\Delta/c + t_i - t_p}{T} - \frac{n}{4} + \frac{n}{2} \tag{6}$$

where t_p is the phase delay time listed in Table 3, T is the period and n is the number of polar passages.   We call ϕ_s the source phase and measure it in parts of a cycle. Δ is the travel distance, c is the phase velocity and Δ/c represents the correction for propagation. t_i is the phase delay time caused by the recording instrument.   Table 4 shows the average value of c for G waves over various great circles obtained by Toksöz and and Anderson.[32]   Table 4 also shows the values of t_i corresponding to the long period seismograph of the $WWSS$ stations computed by the use of Hagiwara's formula[33] on the assumption that the pendulum period is 30 sec, the galvanometer period 100 sec, and both are critically damped.

31) T. HIRASAWA, reported at the meeting of the Seismological Society of Japan, Oct. 1965.

32) M. N. TOKSÖZ and D. L. ANDERSON, report contract AF-AFOSR-25-63, California Inst. Tech., 1963.

33) T. HAGIWARA, Bull. Earthq. Res. Inst., 36 (1958), 139-164.

Table 4. Phase velocity of G waves and instrumental delay
time used for correction

Frequency f $(\sec^{-1})$	Period T (sec)	Phase velocity C (km/sec)	Instrumental phase delay time t_i (sec)
0.0050	200.0	4.901	88
0.0065	153.8	4.774	75
0.0080	125.0	4.697	67
0.0095	105.3	4.642	60
0.0110	90.9	4.604	55
0.0125	80.0	4.575	51

The correction term $-\dfrac{n}{4}$ in the above formula comes from the polar phase advance[34] of $\dfrac{\pi}{2}$ occurring when waves pass through the epicentre or its antipode. Although this value corresponds to a uniform spherical earth model, it will be shown later in the present paper that this is a good first approximation for the actual earth. The last term $\dfrac{n}{2}$ enters in the formula because the source phase ϕ_s is defined in such a way that the counterclockwise motion at the epicentre, when waves departed there, is taken as being positive.

The source phase ϕ_s obtained from G2 and G3 waves are listed in Table 5 according to the azimuth of radiation for periods from 80 to 200 sec. As can be seen in the table, the variability of the value within a small range of radiation azimuth is greater for G3 waves than for G2. The variability increases with frequency for both G2 and G3. For obtaining the orientation of the source double couple, we shall use only the values for G2 waves with period of 200 sec. Analyses of data for G2 waves with shorter periods and for G3 waves will be made later.

For a rough estimation of the amplitude variation with respect to the radiation azimuth, the amplitude spectral densities listed in Table 2 for G2 waves with period 200 sec are equalized to the lapse time of 7000 sec and the epicentral distance of 90°, as shown in Table 6. The Q value is assumed as 120 according to the result of Ben-Menahem and Toksöz.[35] As shown in the table, the correction factor for dissipation is

---

34) J. N. BRUNE *et al.*, *loc. cit.*, 7).
35) A. BEN-MENAHEM and M. N. TOKSÖZ, cited by F. PRESS, *Research in Geophysics*, **2**. Solid Earth and Interface Phenomena (The M. I. T. Press, 1964.)

Table 5. Source phase ϕ_s of G waves referred to counterclockwise motion as seen from the epicentre

Station	Wave type	Radiation azimuth (deg.)	Frequency in c/s					
			.005	.0065	.008	.0095	.0110	.0125
G D H	G2	− 175.3	− .42	− .28	− .24	− .15	− .12	+ .02
T R N	G2	− 154.3	− .07	− .01	− .49	+ .23	+ .33	+ .39
G O L	G2	− 135.4	− .22	− .30	+ .24	+ .29	− .37	− .21
B H P	G2	− 134.3	− .24	− .26	− .14	− .26	− .24	− .20
L P S	G2	− 129.4	− .23	− .33	− .38	− .49	+ .19	+ .12
T U C	G2	− 127.0	− .28	− .40	− .44	+ .37	+ .33	+ .41
G S C	G2	− 125.9	− .23	− .40	+ .44	+ .39	+ .31	− .20
H N R	G2	− 26.6	− .49	− .39	− .39	− .38	− .32	+ .39
G U A	G2	− 13.1	+ .47	+ .46	+ .44	− .49	− .48	+ .44
T A U	G2	− 6.0	+ .32	+ .32	+ .30	+ .19	+ .34	+ .47
A D E	G2	0.4	+ .43	+ .39	− .24	− .27	− .23	− .15
N H A	G2	53.8	− .16	− .20	− .32	− .34	− .34	− .24
H K C	G2	60.5	− .12	− .24	− .39	− .46	+ .44	+ .25
C O P	G2	152.2	+ .42	+ .39	+ .39	− .47	− .47	− .29
P T O	G2	156.2	+ .39	+ .39	+ .37	+ .50	− .40	− .33
E S K	G2	159.4	+ .38	+ .34	+ .34	− .39	− .45	− .35
V A L	G2	161.7	+ .36	+ .32	+ .30	+ .43	− .34	+ .50
K T G	G2	173.4	+ .30	+ .21	+ .11	+ .13	+ .11	+ .04
N O R	G2	176.0	+ .36	+ .37	+ .46	+ .27	− .27	+ .49
G D H	G3	4.7	− .32	− .18	− .19	− .11	− .05	+ .04
O G D	G3	24.9	+ .24	+ .36	+ .44	− .47	− .41	− .45
T R N	G3	25.7	+ .30	− .45	− .41	− .04	+ .12	− .23
C A R	G3	32.0	− .43	+ .36	+ .42	− .49	− .44	+ .41
C O L	G3	32.7	− .13	− .25	− .37	− .42	+ .50	− .49
G O L	G3	44.6	− .26	− .45	+ .35	+ .25	+ .09	.00
B H P	G3	45.7	− .17	− .31	− .46	+ .48	− .48	+ .40
L O N	G3	46.7	− .30	− .46	+ .40	+ .36	+ .38	+ .47
C O R	G3	49.3	− .31	− .47	+ .48	+ .42	+ .50	− .41
L P S	G3	50.6	− .26	− .41	+ .37	+ .21	+ .07	− .04
Q U I	G3	51.2	− .24	− .37	+ .46	+ .36	+ .25	+ .15
T U C	G3	53.0	− .31	− .42	+ .41	+ .41	− .29	− .31
G S C	G3	54.1	− .38	− .36	− .34	− .42	+ .35	− .33
L P B	G3	54.8	− .16	− .27	− .22	− .26	− .39	+ .19
A R E	G3	59.0	− .21	− .42	+ .30	+ .09	− .06	− .08
P E L	G3	86.1	+ .09	+ .25	+ .31	+ .20	− .39	− .11
K I P	G3	88.4	− .05	+ .07	+ .06	+ .18	+ .48	− .29
A F I	G3	128.3	− .44	− .43	− .27	− .34	− .20	− .04
H N R	G3	153.4	− .41	− .42	− .38	− .23	+ .14	+ .42
R A B	G3	161.2	+ .46	+ .42	+ .36	+ .34	+ .25	+ .09
G U A	G3	166.9	+ .40	+ .03	− .11	+ .06	− .01	− .09
T A U	G3	174.0	+ .39	+ .20	+ .04	− .11	− .10	− .06
A D E	G3	− 179.6	− .45	+ .43	+ .30	+ .24	+ .04	− .13
B A G	G3	− 138.1	+ .15	+ .47	− .32	− .11	+ .11	+ .34
S H I	G3	− 67.7	+ .40	+ .12	− .12	− .17	− .37	+ .39
C O P	G3	− 27.8	− .41	− .23	− .18	− .12	− .07	− .05
K O N	G3	− 24.0	− .37	− .34	− .34	− .21	− .07	.00
P T O	G3	− 23.8	− .34	− .26	− .24	− .15	+ .05	+ .07
E S K	G3	− 20.6	− .14	− .28	− .39	− .41	− .11	+ .17
V A L	G3	− 18.3	− .45	− .36	− .42	− .47	+ .30	+ .32
K T G	G3	− 6.6	+ .33	+ .20	+ .11	+ .15	+ .47	− .43
N O R	G3	− 4.0	− .10	+ .25	+ .22	− .06	+ .25	+ .35

Table 6. Amplitude spectral density of G2 waves at period of 200 sec equalized to the lapse time of 7000 sec and the epicentral distance of 90°

Station	Component	Recorded amplitude (Mag: 750)	Group arrival time*	Correction factors			Equalized amplitude spectral density*****
				Instrument** orientation	Geometrical spread***	Dissipation****	
		50 cm sec	7270 sec				52 cm sec
GDH	EW	50	7270	1.02	.98	1.04	52
TRN	EW	48	5877	1.06	.89	.86	38
GOL	EW	30	7052	1.43	1.00	1.01	43
BHP	EW	65	6114	1.22	.93	.89	66
LPS	EW	47	6409	1.28	.97	.92	54
TUC	NS	89	7079	1.35	1.00	1.01	122
GSC	NS	24	7261	1.28	.99	1.03	31
HNR	EW	61	7867	1.08	.88	1.12	65
GUA	EW	113	8529	1.02	.65	1.22	91
TAU	EW	60	7081	1.01	.99	1.01	61
ADE	EW	62	7480	1.00	.98	1.06	64
NHA	EW	114	8236	1.30	.77	1.17	134
HKC	EW	76	8565	1.49	.67	1.23	92
COP	EW	80	7203	1.32	.98	1.03	107
PTO	EW	101	6705	1.10	1.00	.96	107
ESK	EW	69	7077	1.14	.99	1.01	79
VAL	EW	74	6896	1.09	1.00	.99	79
KTG	EW	119	7409	1.04	.98	1.05	128
NOR	EW	50	7749	1.08	.93	1.11	56

*   Average of group delay times for periods 200 to 80 sec.

** $1/\cos\theta$, where θ is the departure of the instrument orientation from the transverse direction to the great circle.

*** $\sqrt{\sin\Delta}$, where Δ is the epicentral distance.

**** $\exp\{\pi(t_g-7000)/QT\}$, where t_g is the group arrival time, and T is the period. Q is assumed as 120.

***** Referred to the recorded amplitude (normalized to magnification 750) without instrumental correction.
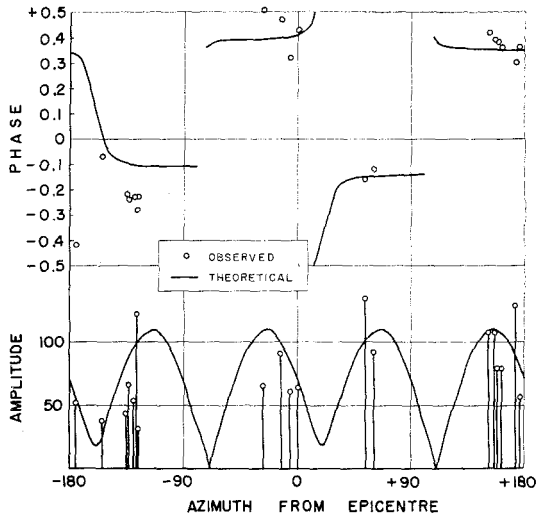
Fig. 3 Comparison of the theoretical source phase (refers to counterclockwise motion as seen from epicentre) and amplitude with the observed for G2 waves with period of 200 sec. The theoretical curves are computed for a double couple source corresponding to pure reverse dip-slip fault striking N20°E with the dip angle of 65°. The unit of amplitude is arbitrary. The absolute value of amplitude is discussed in Part 2.

close to unity and a different choice of Q value will cause a negligible effect on the corrected values.

The source phase and amplitude thus obtained for various azimuths from the epicentre are shown in Fig. 3. Theoretical curves shown in the figure fit well the observed points both for phase and amplitude. These theoretical curves[36] are based on a double couple model corresponding to a reverse fault striking in N20°E. (The theoretical curves for a single couple are nearly the same as those for a double couple in the case of pure dip slip, the difference showing up in the radiation patterns of S and Rayleigh waves in such a case.) The fault plane is either the one dipping toward N70°W with dip angle of 65° or the one dipping toward N110°E with dip angle of 25°. In any case, the fault motion is upward on the overhanging side of the plane. As mentioned in the introduction, the field investigation made in the epicentral area indicated the fault strike running in the direction N20° to 30°E, which agrees remarkably well with the one obtained from G waves. From the field observations

36) K. AKI, loc. cit., 17).

that the northwest part of the area was upheaved and the southeast part subsided, the fault plane which is dipping toward N70°W is preferred.

It must be mentioned that the above solution is not a unique one that explains the observation on *G* waves. The dip angle of the fault plane may be varied considerably with negligible change in the theoretical phase curve and the pattern of azimuthal dependence of amplitude. Furthermore, a strike slip faulting along a vertical fault striking either N25°W or N65°E can explain the observed phase and amplitude. This interpretation, however, contradicts the radiation pattern of the first motion of *P* waves observed at local and world-wide seismograph stations.

§ 4. Comparison with the radiation pattern of the first motion.

For a precise determination of the emergence angle of ray that reaches a local station as the first arrival, we must know accurately the focal depth and the local crustal structure. By the use of the *P* time data supplied from the *JMA*, the focal depth was computed for three crustal models, in which the velocity distribution is assumed as $v = v_0(r/r_0)^{z_0}$ for the crust and $v = v_1(r/r_1)^{z_1}$ for the mantle, where r is the distance from the earth's centre. In all the models,[37] v_0 is 5.78 km/sec, v_1 is 7.75 km/sec, z_0 is -24.4 and z_1 is -2.3. The crustal thickness, $r_0 - r_1$, is varied from 29 to 35 km and we obtained the focal depth varying from 10.6 to 18.6 km as shown in Table 7. This is another example in which the focal depth determined by the *JMA* (40 km in this case) is a little too deep.[38]

Table 7. Origin time, epicentre and focal depth under different assumption on crustal thickness

Crustal thickness (km)	Origin time (sec)	Latitude (deg)	Longitude (deg)	Focal depth (km)
29	40.8±0.47	38.41±.016	139.23±.020	10.6±4.4
32	40.6±0.43	38.41±.016	139.23±.020	13.8±4.1
35	40.6±0.39	38.41±.016	139.23±.020	18.6±3.9
J M A	39.9	38.350	139.183	40.0
C G S	44.3	38.3	139.1	57

37) K. AKI, *Bull. Earthq. Res. Inst.*, **43** (1965), 15–22.
38) K. AKI, *Bull. Earthq. Res. Inst.*, **43** (1965), 23–38.

UPPER   FOCAL   HEMISPHERE
OF
THE   NIIGATA   EARTHQUAKE
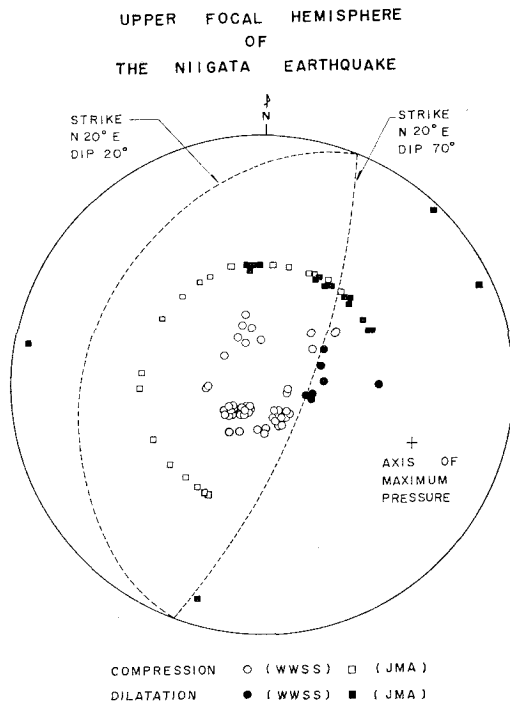
Fig. 4 Stereographic projection of the upper focal hemisphere
for the Niigata earthquake.

The upper focal hemisphere is shown by a stereographic projection
in Fig. 4.   Nearly identical patterns of compression and dilatation are
obtained in the above three cases of different crustal thickness.   The
first motion data from the *WWSS* stations listed in Table 1 are also
included in Fig. 2.   Two mutually orthogonal planes which best separate
compressions from dilations are drawn by the use of the Wulff's grid.[39]
The strike of both planes runs in the direction N20°E, identical to the
one found from the *G* wave data.   The fault plane is either the one
dipping toward N70°W with dip angle of 70° or the one dipping toward
N110°E with dip angle of 20°.   In any case, the motion direction is up-
ward on the overhanging side of the fault in agreement with the result
obtained from *G* waves.

39) E. N. BESSONOVA *et al.*, *Investigation of the Mechanism of Earthquakes* (1960),
p. 151.

§ 5. Variability of amplitude spectra of G waves.

As shown in the preceding sections, the mechanism of G wave generation at the source was successfully restored from the observed amplitude and phase of $G2$ waves with period of 200 sec. We noticed, however, that even at this long period the amplitude show relatively greater variability within a very narrow range of radiation azimuth than the phase. The variability increases with decreasing period. In this section, we shall choose a group of stations located in a limited range of radiation azimuth, and examine the variability of amplitude spectral density within the group.

Stations are grouped into three; one is in the azimuthal range from 0 to 45° centred at about N20°E, which is the theoretical node direction for G waves (For convenience, we call it node direction although this is not a true node as shown in Fig. 3.), the other two groups cover two opposite azimuthal ranges 0 to $-30°$ and 180° to 150°, both in the loop direction for G waves. The stations of these groups are shown in Tables 8 and 9. Table 8 lists the amplitude spectral densities of $G2$ waves equalized to the lapse time of 7000 sec and the epicentral distance of 90°. Table 9 lists those of $G3$ waves equalized to the lapse time of 11000 sec and the epicentral distance of 90°. The equalization procedure is the same as illustrated in Table 6. We used the same Q value of 120 for all the frequencies. A different choice of Q value will affect only slightly the equalized values, because the time differences between the group arrival time and the equalized time (7000 sec for $G2$ and 11000 sec for $G3$) are small for any stations.

As shown in these tables, the value of amplitude varies considerably among the stations of each group. As a measure of the variability, we estimate the variance σ^2 according to the following formula.

$$\sigma^2 = \frac{\sum (x_i - \bar{x})^2}{n-1} , \qquad (7)$$

where x_i is the spectral density at the ith station of group, $\bar{x} = \sum x_i/n$, and n is the number of stations of the group. The mean and variance for $G2$ waves are listed in Table 10 and those for $G3$ waves in Table 11.

First, we shall compare the variances for the two opposite loop directions (Group 1 and 2 in Table 10, Group 5 and 6 in Table 11). We notice in general that the variance increases with decreasing period. There seems no significant difference in the variance between Groups 1 and 2. In fact,

Table 8. Amplitude spectral density of *G2* waves equalized to the
lapse time of 7000 sec and the epicentral distance of 90°
(unit in cm sec on the record with magnification 750, without instrumental correction)

Group No.*	Station		Radiation azimuth	$f=.005$ c/s $T=200$ sec	.0065 154	.0080 125	.0095 105	.0110 91	.0125 80	.0140 71	.0155 65	.0170 59	.0185 54	.0200 50
4	GDH	near node	−175.3°	51	96	144	165	154	171	170	146	181	204	116
	TRN		−154.3	36	65	117	152	168	174	175	194	171	76	16
	GOL		−135.4	42	52	35	59	29	134	153	95	83	76	31
	BHP		−134.4	65	65	30	59	128	119	138	128	22	59	31
1	HNR	near loop	− 26.6	60	92	153	246	202	208	212	164	81	313	23
	GUA		− 13.1	89	161	155	106	112	146	152	104	49	85	66
	TAU		− 6.0	60	90	69	61	47	104	31	38	90	48	46
	ADE		0.4	64	21	64	189	198	49	107	165	23	33	88
2	COP	near loop	152.2	81	103	55	54	64	55	80	25	56	94	62
	PTO		156.2	97	98	68	79	145	193	222	212	136	40	25
	ESK		159.4	69	89	70	23	77	134	141	68	116	105	35
	VAL		161.7	73	87	129	100	31	11	69	93	60	37	41
	KTG		173.4	123	171	256	289	231	194	189	124	54	72	82

* Corresponds to the group number in Table 10.

Table 9. Amplitude spectral density of G3 waves equalized to the lapse time of 11000 sec and the epicentral distance of 90°

(unit in cm sec on the record with magnification 750, without instrumental correction)

Group No.*		Station	Radiation azimuth	$f = .005$ c/s $T = 200$ sec	.0065 154	.0080 125	.0095 105	.0110 91	.0125 80	.0140 71	.0155 65	.0170 59	.0185 54	.0200 50
8	near node	GDH	4.7°	25	38	50	47	52	24	21	20	16	14	12
		OGD	24.9	26	35	52	58	40	18	17	25	20	3	0
		TRN	25.7	12	44	46	36	19	14	57	29	40	31	14
		CAR	32.0	44	60	65	62	49	27	25	26	15	2	8
		COL	32.7	84	131	168	164	70	13	47	23	5	5	10
		GOL	44.6	15	34	43	20	19	6	17	45	15	25	8
		BHP	45.7	44	58	61	41	49	62	36	11	6	11	9
6	near loop	HNR	153.4	50	88	53	55	69	36	21	12	34	15	18
		RAB	161.2	264	218	153	92	43	26	40	60	57	35	21
		GUA	166.9	25	21	17	28	34	29	31	32	25	14	7
		TAU	174.0	41	44	34	27	16	28	13	21	27	40	2
		ADE	−179.6	38	31	22	15	29	44	46	20	0	18	17
5	near loop	COP	− 27.8	36	40	73	51	52	66	22	40	12	16	24
		KON	− 24.0	57	33	36	66	41	42	28	26	49	25	18
		PTO	− 23.8	45	43	46	23	49	82	87	41	20	9	21
		ESK	− 20.6	43	48	59	32	7	72	46	27	17	18	13
		VAL	− 18.3	23	21	51	35	38	53	64	37	28	19	18
		KTG	− 6.6	42	49	43	30	22	24	40	34	27	7	8

* Corresponds to the group number in Table 11,

Table 10. Comparison of the mean and variance of amplitude spectral density of G2 waves among different station groups

Group		1 ($-30°$ to $0°$, $n_1=4$)		Comparison between group 1 and 2		2 ($150°$ to $180°$, $n_2=5$)		3 ($-30°$ to $0°$, $150°$ to $180°$)			4 ($-180°$ to $-135°$, $n=4$)		Comparison between group 3 and 4	
freq. (c/s)	period (sec)	$\bar{x}_1$	σ_1^2	F	t	$\bar{x}_2$	σ_2^2	$\bar{x}_3$	σ_3^2	$\sigma_3/\bar{x}_3$	$\bar{x}_4$	σ_4^2	F	t
.005	200	68.3	194.9	$2.488 < F_3^4$ *	$1.595 < t_7$ **	88.6	484.9	79.5	360.4	0.24	48.5	159.1	$2.265 < F_3^7$ *	$2.978 > t_{10}$ **
.0065	154	91.0	3267.	$2.676 < F_4^3$	$0.606 < t_7$	109.6	1221.	101.3	2097.	0.45	69.5	349.7	$5.997 < F_3^7$	$1.334 < t_{10}$
.0080	125	110.3	2557.	$2.729 < F_3^4$	$0.120 < t_7$	115.6	6977.	113.2	4351.	0.58	81.5	3326.	$1.308 < F_3^7$	$0.829 < t_{10}$
.0095	105	150.5	6863.	$1.596 < F_3^4$	$0.645 < t_7$	109.0	10951.	127.4	9196.	0.75	108.7	3328.	$2.763 < F_3^7$	$0.361 < t_{10}$
.0110	91	139.8	5546.	$1.141 < F_3^4$	$0.582 < t_7$	109.6	6328.	123.0	5991.	0.63	119.8	3935.	$1.523 < F_3^7$	$0.073 < t_{10}$
.0125	80	126.8	4511.	$1.501 < F_3^4$	$0.184 < t_7$	117.4	6769.	121.6	5799.	0.63	149.5	743.9	$7.795 < F_3^7$	$0.655 < t_{10}$
.0140	71	125.5	5818.	$1.309 < F_4^3$	$0.309 < t_7$	140.2	4444.	133.7	5030.	0.53	159.0	284.6	$17.67 > F_3^7$	—
.0155	65	117.8	3640.	$1.354 < F_3^4$	$0.302 < t_7$	104.4	4930.	110.3	4376.	0.60	140.8	1706.	$2.565 < F_3^7$	$0.849 < t_{10}$
.0170	56	60.8	942.9	$1.588 < F_3^4$	$0.992 < t_7$	84.4	1497.	73.9	1259.	0.48	114.3	5720.	$4.544 > F_7^3$	—
.0185	54	119.8	17040.	$17.97 > F_4^3$	—	69.6	948.3	64.3***	871.***	0.46	103.8	4531.	$5.202 > F_6^3$	—
.0200	50	55.8	770.8	$1.472 < F_4^3$	$0.404 < t_7$	49.0	523.5	52.0	629.3	0.50	48.5	2074.	$3.296 < F_3^7$	$0.179 < t_{10}$

* $F_3^4(0.05)=9.117$, $F_4^3(0.05)=6.591$, $F_4^3(0.05)=4.347$, $F_7^3(0.05)=8.887$ and $F_6^3(0.05)=4.757$.

** $t_7(0.05)=2.365$ and $t_{10}(0.05)=2.228$.

*** HNR excluded.

Table 11. Comparison of the mean and variance of amplitude spectral density of G3 waves among different station groups

Group		5		6		Comparison between group 5 and 6		7			8		Comparison between group 7 and 8	
Radiation azimuths		$-30°$ to $0°$ $n=6$		$150°$ to $180°$ $n=4^*$				$-30°$ to $0°$ $150°$ to $180°$			$0°$ to $45°$ $n=6^{**}$			
freq.	period	$\bar{x}_5$	σ_5^2	$\bar{x}_6$	σ_6^2	F	t	$\bar{x}_7$	σ_7^2	$\sigma_7/\bar{x}_7$	$\bar{x}_8$	σ_8^2	F	t
(c/s) .005	(sec) 200	41.0	125.2	38.5	107.1	*** $1.169 < F^5_3$	**** $0.358 < t_8$	40.0	118.4	0.27	27.7	189.9	*** $1.604 < F^8_5$	**** $1.971 < t_{13}$
.0065	154	39.0	111.6	46.0	872.6	$7.814 > F^3_5$	—	41.8	397.0	0.48	44.8	132.9	$2.987 < F^8_5$	$0.338 < t_{13}$
.0080	125	51.3	172.3	31.5	256.4	$1.488 < F^3_5$	$2.150 < t_8$	43.4	203.9	0.33	52.8	73.3	$2.782 < F^8_5$	$1.468 < t_{13}$
.0095	105	39.5	254.8	31.3	285.6	$1.121 < F^3_5$	$0.778 < t_8$	36.2	266.4	0.45	44.0	235.6	$1.131 < F^8_5$	$0.947 < t_{13}$
.0110	91	34.8	296.5	37.0	513.0	$1.949 < F^3_5$	$0.175 < t_8$	35.7	377.6	0.54	38.0	232.8	$1.622 < F^8_5$	$0.251 < t_{13}$
.0125	80	56.5	452.0	34.3	54.9	$8.234 < F^5_3$	$1.976 < t_8$	47.6	303.1	0.36	25.2	380.9	$1.257 < F^8_5$	$2.378 > t_{13}$
.0140	71	47.8	584.1	27.8	202.2	$2.889 < F^5_3$	$1.477 < t_8$	39.8	441.0	0.53	28.8	240.1	$1.837 < F^8_5$	$1.117 < t_{13}$
.0155	65	34.2	41.3	21.3	67.6	$1.637 < F^3_5$	$2.794 > t_8$	29.0	51.3	0.25	26.0	126.4	$2.464 < F^8_5$	$0.648 < t_{13}$
.0170	59	25.5	169.2	21.5	66.3	$2.552 < F^5_3$	$0.542 < t_8$	23.9	130.6	0.48	18.7	142.9	$1.094 < F^8_5$	$0.884 < t_{13}$
.0185	54	15.7	44.7	21.8	150.9	$3.376 < F^3_5$	$1.034 < t_8$	18.1	84.5	0.51	14.3	136.7	$1.618 < F^8_5$	$0.724 < t_{13}$
.0200	50	17.0	32.8	11.0	60.7	$1.851 < F^3_5$	$1.413 < t_8$	14.6	43.3	0.45	8.5	23.2	$1.866 < F^8_5$	$1.980 < t_{13}$

* RAB excluded.

** COL excluded.

*** $F^5_3(0.05)=9.014$, $F^3_5(0.05)=5.410$, $F^8_5(0.05)=4.818$ and $F^5_8(0.05)=3.688$.

**** $t_8(0.05)=2.306$, $t_{13}(0.05)=2.160$.

the F value, that is, the ratio of the estimate of variance of one group to that of the other does not exceed the rejection limit on the significance level of 5% at all periods with only two exceptions; 54 sec for $G2$ and 154 sec for $G3$. Except for these two cases, we may compare the mean of amplitude spectral densities between the two groups by the use of Student's "t", which is defined as follows,

$$t = \frac{\dfrac{\bar{x}_1 - \bar{x}_2}{(1/n_1 + 1/n_2)^{1/2}}}{\left\{ \dfrac{(n_1-1)\sigma_1^2 + (n_2-1)\sigma_2^2}{n_1+n_2-2} \right\}^{1/2}} \tag{8}$$

where the suffix refers to the group number. This quantity obeys the t-distribution with $n_1 + n_2 - 2$ degrees of freedom. For instance, the probability that the t value exceeds 2.365 is 0.05 if the number of degrees of freedom is 7. As shown in Table 10, none of the t values for $G2$ waves exceeds this limit. Thus, we cannot reject, on the 5% significance level, the hypothesis that these two groups belong to the same statistical ensemble. This result permits us to put them together as Group 3. The mean and variance of this group are then computed by

$$\bar{x}_3 = \frac{n_1\bar{x}_1 + n_2\bar{x}_2}{n_1+n_2} \tag{9}$$

$$\sigma_3^2 = \frac{(n_1-1)\sigma_1^2 + (n_2-1)\sigma_2^2}{n_1+n_2-2} \ , \tag{10}$$

and listed in Table 2. We shall now compare these values with those expected for the spectral density of a random wavelet.

We define a random wavelet as a finite portion of the Gaussian noise which is smoothed by a linear realizable filter with a transfer function $G(\omega)$. Let x_i $(i=1, 2, \cdots, n)$ be the displacement of the wavelet from zero sampled at equal intervals of Δt. The Fourier cosine and sine integrals may be approximated by

$$a_j = \Delta t \sum_i x_i \cos (\omega_j i \Delta t) \tag{11}$$

and

$$b_j = \Delta t \sum_i x_i \sin (\omega_j i \Delta t) \tag{12}$$

respectively. Since these expressions are weighted averages of x_i, their

mean and variances are related to the mean and variance of x_i by well known formulas. We obtain

$$\overline{a_j} = 0 , \tag{13}$$

$$\overline{b_j} = 0 , \tag{14}$$

$$\overline{a_j^2} \simeq \frac{n \Delta t^2}{2} \, | \, G(\omega_j) \, |^2 \sigma_g^2 \tag{15}$$

$$\overline{b_j^2} \simeq \frac{n \Delta t^2}{2} \, | \, G(\omega_j)^2 \, | \sigma_g^2 \tag{16}$$

where σ_g^2 is the variance of the Gaussian noise before smoothing. The amplitude spectral density of the random wavelet is the square root of the sum of a_j^2 and b_j^2. Since a_j and b_j obeys the Gaussian distribution with zero mean value and a common variance, the sum of their squares devided by the variance obeys the χ^2 distribution with two degrees of freedom. Putting $A_j^2 = a_j^2 + b_j^2$, we obtain the probability density function of the amplitude spectral density A_j as

$$f(A_j) = \frac{A_j}{\sigma_j^2} \, \exp \left(- \frac{A_j^2}{2\sigma_j^2} \right) , \tag{17}$$

where

$$\sigma_j^2 = \frac{n \Delta t^2}{2} \, | \, G(\omega_j) \, |^2 \sigma_g^2.$$

The mean and variance of A_j are then obtained as

$$\overline{A_j} = \int_0^\infty A_j f(A_j) dA_j = \sqrt{\frac{\pi}{2}} \, \sigma_j \tag{18}$$

$$\overline{(A_j - \overline{A_j})^2} = \int_0^\infty (A_j - \overline{A_j})^2 f(A_j) dA_j = \left(2 - \frac{\pi}{2} \right) \sigma_j^2 \tag{19}$$

In comparing these theoretical values with the observed, it is convenient to form the ratio of the square root of variance to the mean as a measure of variability. The theoretical ratio is

$$\frac{\sqrt{\overline{(A_j - \overline{A_j})^2}}}{\overline{A_j}} = \frac{\sqrt{2 - \dfrac{\pi}{2}}}{\sqrt{\dfrac{\pi}{2}}} = 0.523 . \tag{20}$$
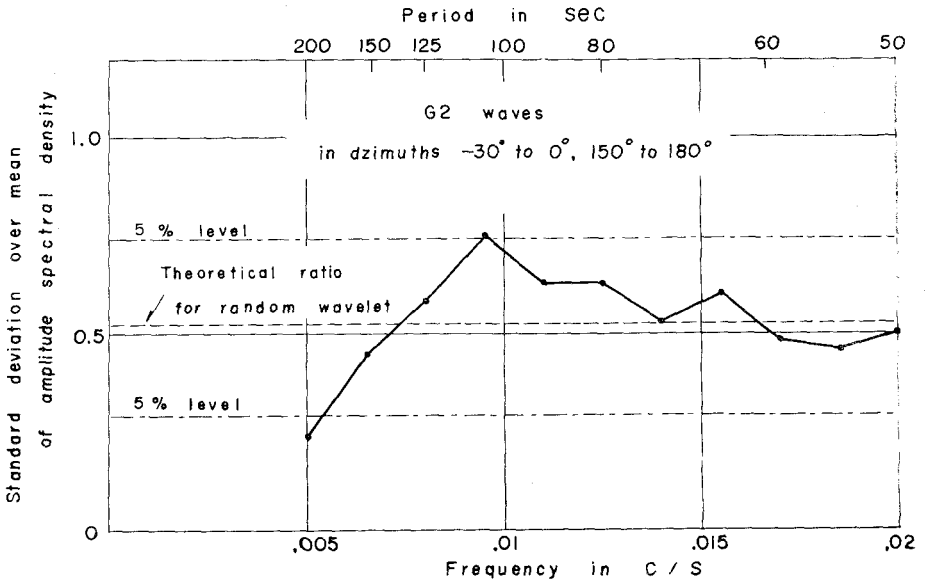
Fig. 5   The ratio of square root of sample variance to sample mean for amplitude spectral density of the equalized $G2$ waves in the radiation azimuths $-30°$ to $0°$, and $150°$ to $180°$. The upper and lower limits indicate the range of the ratio where the hypothesis of random wavelet is not rejected on the 5% significance level.

The corresponding observed ratios for Group 3 of $G2$ waves are given in Table 10 and plotted against period in Fig. 5.   The ratio is the smallest at 200 sec, approaches to the theoretical value of 0.523 at 150 sec and reaches 0.75 at 105 sec.   At shorter periods, the ratio lies within 0.1 from the theoretical value.   The limits for observed values significantly departing from the theoretical may be obtained as follows.

We roughly assume that the observed spectral density approximately obeys a Gaussian distribution.   Then, the sample variance σ^2 multiplied by the number of degrees of freedom and devided by the ensemble variance σ_e^2 will obey the χ^2 distribution with that number of degrees of freedom. We roughly estimate the ensemble variance σ_e^2 from the sample mean $\bar{x}$ by the following relation

$$\sigma_e^2 \doteqdot (0.523\bar{x})^2 \ . \tag{21}$$

It then follows that $n\sigma^2/(0.523\bar{x})^2$ obeys the χ^2 distribution with n degrees of freedom.   For Group 3 of $G2$ waves, the number of degrees of freedom is 7, in which case the rejection limits of χ^2 on the significance level of 5% are 2.1674 and 14.067.   The rejection limits of the ratio

$\sigma/\bar{x}$ are then $0.523\sqrt{2.1674/7}=0.291$ and $0.523\sqrt{14.067/7}=0.741$. The upper limit thus obtained may not be applicable because the great sample variance contradicts the assumption that the spectral density obeys the Gaussian distribution. We may, however, use the lower limit in our problem. The observed ratio of 0.24 at period of 200 sec is lower than the limit 0.291. For other periods the observed ratios are greater than this limit. From this we conclude that except for 200 sec, the amplitude spectral density of $G2$ waves may be regarded as those of a random wavelet.

The same analysis on $G3$ waves leads to a similar result, as shown in Table 11 and Fig. 6. We notice, however, that the variability is in general less for $G3$ waves than for $G2$ waves, and the randomness is rejected not only at period of 200 sec but also at 65 sec.

This difference in variability between $G2$ and $G3$ waves is shown more directly in the histograms of spectral density in Figs. 7 and 8.

In Fig. 7, we show the number of cases in which the spectral density of $G2$ waves with periods from 65 to 125 sec falls in a specified range, after confirming, by the "t" and "F" tests, that the mean and
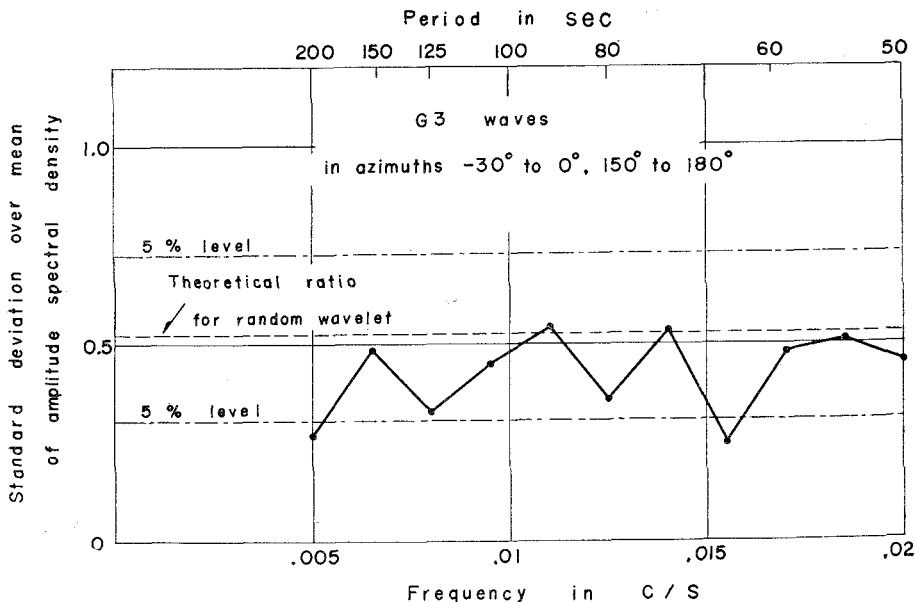
Fig. 6 The ratio of square root of sample variance to sample mean for amplitude spectral density of the equalized $G3$ waves in the radiation azimuths $-30°$ to $0°$, and $150°$ to $180°$. The upper and lower limits indicate the range of the ratio where the hypothesis of random wavelet is not rejected on the 5% significance level.
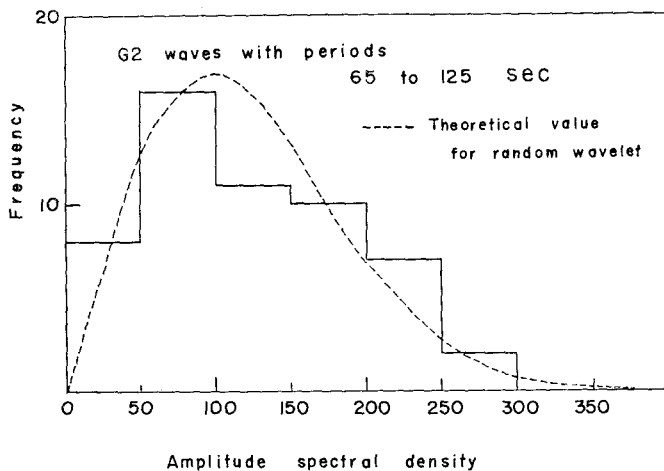
Fig. 7.   Comparison of the histogram of amplitude spectral density
of the equalized *G*2 waves with the theoretical value for random
wavelet.
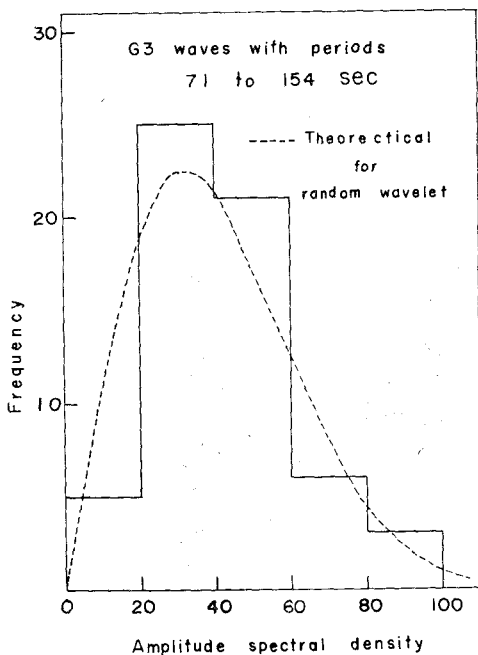
Fig. 8   Comparison of the histogram of amplitude spectral
density of the equalized *G*3 waves with the theoretical value
for random wavelet.

variance are uniform in the above period range.   For $G3$ waves, we can put the data for periods from 71 to 154 sec together, and obtain the histogram as shown in Fig. 8.   The theoretical probability density curves in both figures are computed by Eq. 17, where the theoretical variance is computed from the sample mean by Eq. 21.   The agreement between the observed and theoretical curves is good for both cases.

Now, we shall make a comparison of the variability of spectral density between the theoretical node and loop directions.   Group 4 in Table 10 and Group 8 in Table 11 includes the stations in the azimuthal range from 0° to 45°, which lie within 25° from the theoretical nodal line indicated in Fig. 3.   The mean and variance for this group are listed in the tables.   The comparison of mean is made for periods, for which no significant difference in variance is found by the "F" test.
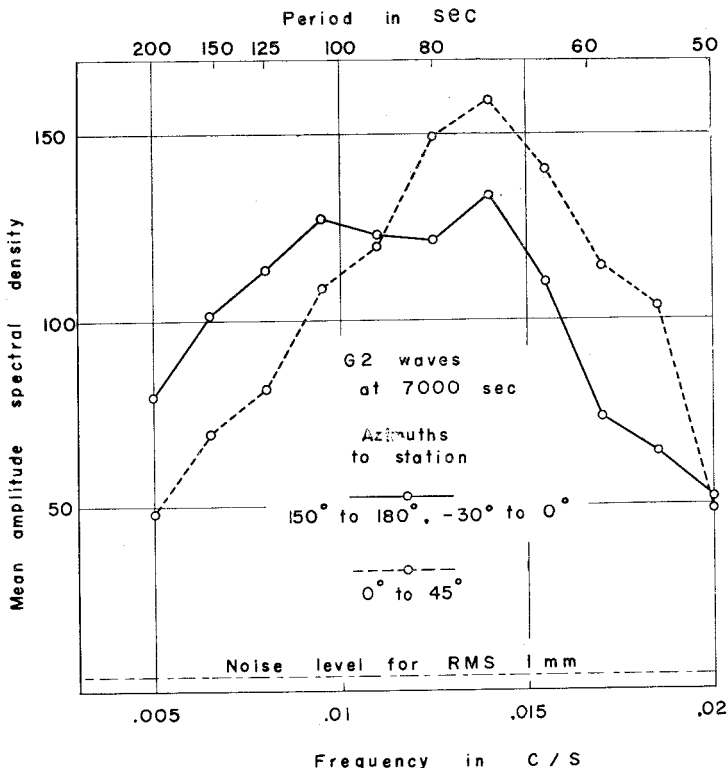
Fig. 9   Mean amplitude spectral density of the equalized $G2$ waves in the loop direction (−30° to 0°, and 150° to 180°) and in the node direction (0° to 45°).   The noise level indicated corresponds to a Gaussian noise (not smoothed) with root-mean-square amplitude of 1 mm on the record. (cf. §2.)

For *G*2 waves, we found that only at period of 200 sec the mean amplitude spectral density in the theoretical loop direction (Group 3) is significantly greater than that in the node direction (Group 3). As a matter of fact, as shown in Fig. 9 the mean density is greater in the node direction than in the loop direction for periods shorter than 80 sec, although the difference is not significant on the level of 5%. This reversal occurrs at a longer period (150 sec) for *G*3 waves as shown in Fig. 10. For *G*3 waves, a significant difference is observed only at period of 80 sec, at which the spectral density is greater in the theoretical loop direction than in the node direction.
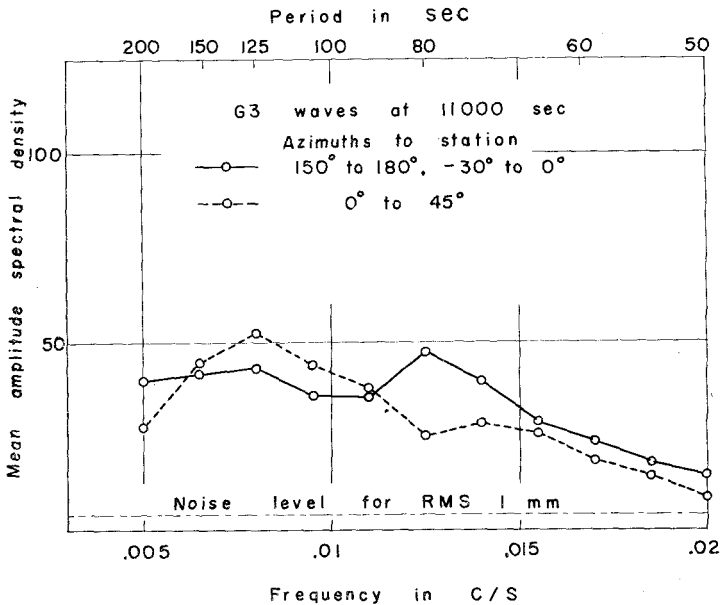
Fig. 10 Mean amplitude spectral density of the equalized *G*3 waves in the loop direction (−30° to 10°, and 150° to 180°) and in the node direction (0° to 45°). The noise level indicated corresponds to a Gaussian noise (not smoothed) with root-mean-square amplitude of 1 mm on the record. (cf. §2.)

It should be remarked here again that the above node direction is not the direction of true node, but shows (Fig. 3) a small finite amplitude which depends on the focal depth, wave length, source orientation and layer parameters of crustal structure. It is, however, difficult, if not impossible, to explain the above observations in terms of these factors as far as a spherically symmetric earth model is assumed.

§ 6. Variability of phase spectra of G waves.

In this section, we shall examine the variability of phase spectra of $G2$ and $G3$ waves. The material is the source phase obtained from observed phase by correcting for propagation and recording. We shall deal only with stations in the loop direction, because a greater variability of phase is theoretically expected near the node direction, and we are interested in the variability where it is expected to be small.

We have selected five stations lying in azimuths from $-30°$ to $0°$ where both $G2$ and $G3$ are well recorded. Table 12 shows the source phase for these stations. For a random wavelet, the probability density function of the phase will take a constant value over the entire range, which we define from $-.5$ to $+.5$. We transform the phase φ_s into a variable y which obeys a Gaussian distribution with zero mean and unit variance by the following formula

$$\int_{-0.5}^{\varphi_s} d\varphi_s = \frac{1}{\sqrt{2\pi}} \int_{-\infty}^{y} \exp(-y^2/2) dy . \tag{22}$$

The transformed values are also listed in Table 12.

In order to find if the observed phases may be regarded as those of a random wavelet, we compute the following quantity for each period and wave type,

$$\chi^2 = \sum_{i=1}^{5} (y_i - \bar{y})^2 , \tag{23}$$

where

$$\bar{y} = \sum_{i=1}^{5} y_i / 5 . \tag{24}$$

If the waves are random, we expect that the above χ^2 will obey the χ^2 distribution with four degrees of freedom.

The results are shown in Fig. 11, where the χ^2 are plotted against period for $G2$ and $G3$ waves. For $G2$ waves, the hypothesis of random wavelet is rejected at periods longer than about 110 sec on the significance level of 5%. On the other hand, for $G3$ waves we cannot reject the hypothesis at all the periods. In other words, the source phase derived from $G3$ waves recorded at stations in a azimuthal range of about 30° from epicentre are so variable that the waves may be regarded as random wavelets. We shall discuss some consequence of this result in the next

Table 12. List of source phase and transformed variable

Station	Wave type	freq. .005 c/s period 200 sec		.0065 c/s 154 sec		.0080 c/s 125 sec		.0095 c/s 105 sec		.0110 c/s 91 sec		.0125 c/s 80 sec	
		φ_s	y	φ_s	y	φ_s	y	φ_s	y	φ_s	y	φ_s	y
C O P	G2	.42	1.40	.39	1.22	.39	1.22	$-$.47	$-$1.88	$-$.47	$-$1.88	$-$.29	$-$0.80
P T O	G2	.39	1.22	.39	1.22	.37	1.12	$-$.50	$-$2.57*	$-$.40	$-$1.28	$-$.33	$-$0.95
E S K	G2	.38	1.17	.34	0.99	.34	0.99	$-$.39	$-$1.22	$-$.45	$-$1.64	$-$.35	$-$0.65
V A L	G2	.36	1.08	.32	0.91	.30	0.84	.43	1.47	$-$.34	$-$0.99	$-$.50	$-$2.57*
K T G	G2	.30	0.84	.21	0.55	.11	0.27	.13	0.33	.11	0.27	.04	0.10
C O P	G3	$-$.41	$-$1.34	$-$.23	$-$0.61	$-$.18	$-$0.46	$-$.12	$-$0.30	$-$.07	$-$0.17	$-$.05	$-$0.12
P T O	G3	$-$.34	$-$0.99	$-$.26	$-$0.70	$-$.24	$-$0.64	$-$.15	$-$0.38	.05	0.12	.07	0.17
E S K	G3	$-$.14	$-$0.35	$-$.28	$-$0.77	$-$.39	$-$1.22	$-$.41	$-$1.34	$-$.11	$-$0.27	.17	0.43
V A L	G3	$-$.45	$-$1.64	$-$.36	$-$1.08	$-$.42	$-$1.40	$-$.47	$-$1.88	.30	0.84	.32	0.91
K T G	G3	.33	0.95	.20	0.52	.11	0.27	.15	0.38	.47	1.88	$-$.43	$-$1.47

* This value corresponds to $\varphi_s = -0.495$.
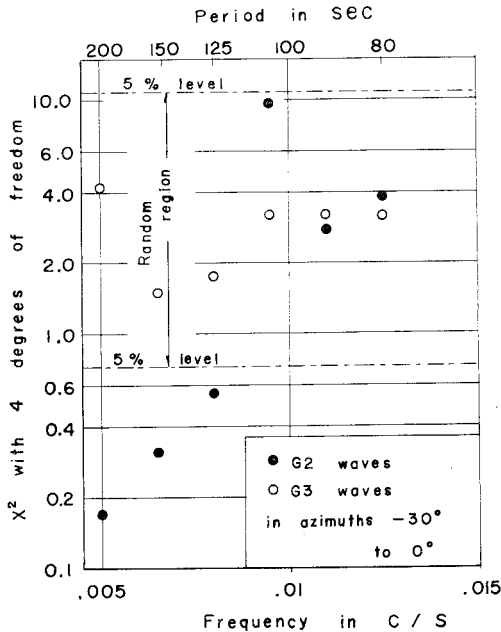
Fig. 11   A test of the hypothesis of random wavelet for
phase angle of $G2$ and $G3$ waves.

section.   At least, this offers a quantitative explanation why we did not
use the $G3$ and short period $G2$ wave data in obtaining the source
mechanism in § 3.

§ 7.   Discussions on the variability of spectra.

We shall now look into the cause of the variability of spectra des-
cribed in the preceding two sections.   At least, we can positively state
that the variability is not due to poor calibration of instruments, because
the variability of both phase and amplitude decreases with increasing
period, and the randomness is rejected for $G2$ waves with period of
200 sec.   We may attribute the randomness of shorter period $G2$ and $G3$
waves to 1) complexity of the source, 2) interference between the waves
undergoing refractions due to lateral heterogeneity of the earth's upper
part, including the complex phenomena of polar passage, and 3) inter-
ference with body waves and higher mode surface waves.
The last factor, which we may call a radial interference as compared
with the lateral one (the second factor), is included because this seems
to explain most readily the smaller amplitude variability of $G3$ waves

relative to $G2$. This may be explained, however, by a lateral interference
alone as follows. If the waves are coherent when they leave the epicentre
and lose the coherency as they travel, the coherency of interfering
waves will be greater for $G2$ waves than for $G3$. The result of inter-
ference between coherent waves can be more variable than that of well-
randomized waves, as most impressively shown on a picture illuminated
by a coherent light from a laser.

It should be remarked here that the observed variability refers to
the azimuthal range of 30° from epicentre. If the randomness applies
to an infinitesimally small range of azimuth, the waves will propagate in
random directions and not in a single direction like the great circle. The
observation of $G3$, $G4$ and $G5$ arriving at right times at many stations
obviously rejects this supposition. Therefore, the variability should
decrease if the azimuthal range be taken narrower.

Our result on the spectral variability throws a serious doubt on the
dependability of the directivity function obtained from a single station
record. Figs. 12 and 13 show the ratio of $G2$ to $G3$ amplitude for stations
in the azimuthal ranges from $-30°$ to $0°$ and from $150°$ to $180°$. The
Q values used for propagation correction are obtained from the mean
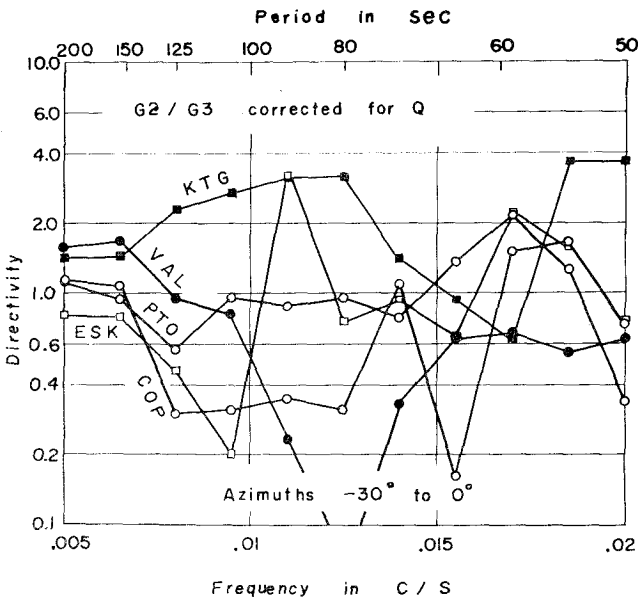
Fig. 12   The directivity functions for the stations located
in the azimuths $-30°$ to $0°$ from the epicentre.
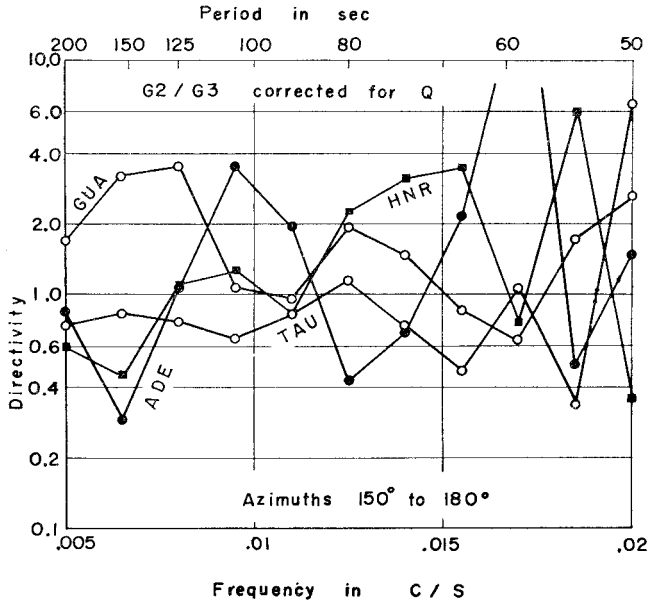
Fig. 13 The directivity functions for the stations located
in the azimuths 150° to 180° from the epicentre.

amplitude, as described in a later section (Column 4, Table 15). These figures show a strong variability of directivity function among stations in a limited azimuthal range.

In order to clarify the cause of the variability of spectra, we shall probably need a denser network of long period seismographs than the existing one. Future efforts must be directed towards finding a deterministic relationship between the spectra at individual stations and the complex factors influencing them. For the present, however, we shall assume that the effect of the complex factors may be eliminated from the observed amplitude spectral density by averaging it over several stations in a certain range of azimuth from epicentre. This assumption may not be too unrealistic, because the chance that the interference phenomena work on amplitude constructively may be equal to the chance that they work destructively. We shall proceed with this assumption to utilize the mean spectral density in a more detailed study of the source mechanism in later sections.

§ 8. Group and phase wave fronts before and after a polar passage.

For a spherically symmetric earth model, the Fourier phase of surface

waves advance by $\pi/2$ when they cross a pole, that is, the epicentre or its antipode. Since the actual earth is not spherically symmetric, the waves will not arrive at a pole simultaneously, and will show a complex interference phenomenon which may not be explained by a simple phase advance.

The pattern of wave fronts just before and after a polar passage may be obtained with a good accurracy by a forward extrapolation of $G2$ waves and a backward extrapolation of $G3$ waves to a small area around the epicentre.

First, we shall find the group wave front that is the position of wave energy at a specified time. Fig. 14 shows the group wave front at 8900 sec after the origin time of earthquake. This was obtained by by extending the position of each station along the great circle direction by the distance over which the waves travel during the time 8900 sec minus the group delay time observed at the stations. The speed of wave
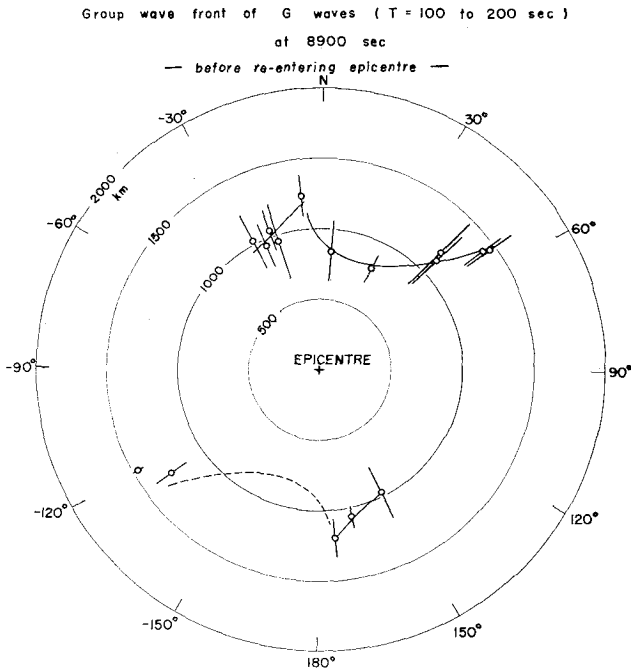
Fig. 14 The group wave front of G waves with periods 100 to 200 sec at 8900 sec after the origin time as extrapolated from $G2$ data. The length of straight line at each extrapolated point indicates the range of standard error.

is assumed as 4.40 km/sec. An error of 1% in this value will produce an error of about 100 km in the extrapolated position of wave front. The group delay time used is the average over periods from 100 to 200 sec. The length of line shown in the figure corresponds to the range of standard error of the average group delay time.

We notice that the earliest arrival occurs at azimuth about N20°E and the latest at about N60°E. Their difference in distance from epicentre is about 700 km which is 1.8% of the total travel distance. Since the maximum difference expected from the ellipticity of the earth is 0.10% at this latitude, the observed difference must be attributed to the lateral variation of wave velocity on the earth. The smoothed curve drawn to fit observed points is exactly point-symmetric about the epicentre. This is expected, since the waves in the opposite azimuths traveled along nearly the same great circle.

Group wave front of G waves (T = 100 to 200 sec)
at 9400 sec
— after passing epicentre —
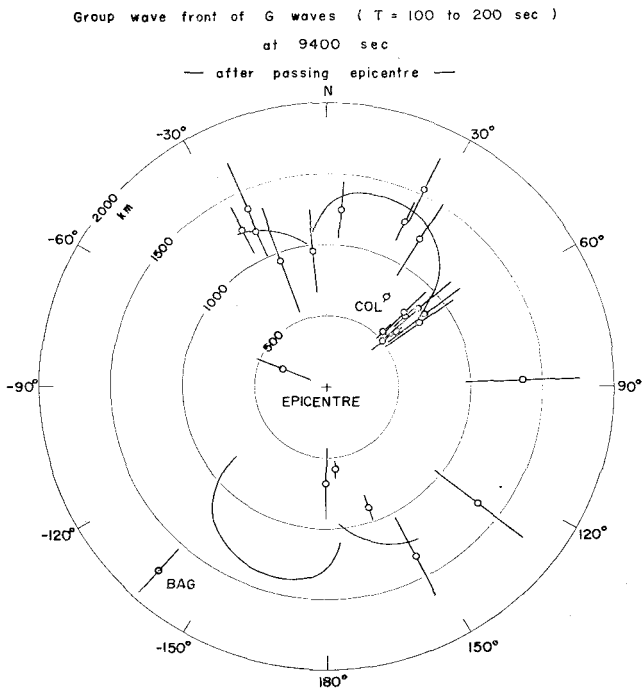
Fig. 15 The group wave front of G waves with periods 100 to 200 sec at 9400 sec after the origin time as extrapolated from G3 data. The curve shows the extrapolation of the smooth curve shown in Fig. 14. The length of straight line at each extrapolated point indicate the range of standard error.

Assuming that the smoothed wave front proceeds with velocity of 4.4 km/sec along the great circle direction passing the epicentre, we may predict a theoretical position of wave front 500 sec later (9400 sec after the origin time). The predicted wave front is compared with the backward extrapolation of $G3$ waves in Fig. 15. The agreement between the predicted and observed is generally good, supporting the simplified assumption made in the prediction. We notice, however, significant discrepancy, for instance, for stations COL and BAG. Both stations show good records of $G3$ waves of typical impulsive form (Fig. 16 and Fig. 17).
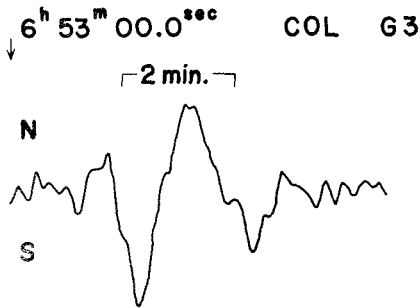
Fig. 16   The record of $G3$ waves at the station COL.

Fig. 17   The record of $G3$ waves at the station BAG.

We cannot attribute this to a poor extrapolation, because both stations are located at relatively short distance from the epicentre. A strong lateral refraction may be a reasonable explanation, because the wave paths to both stations lie along the boundary between the ocean and continent. On the other hand, a significant asymmetry between the NW and SE directions may be attributed to a poor extrapolation, because the wave paths toward SE lie in the Pacific ocean while those toward NW in the Asian continent including the Himalayas.

Keeping in mind the picture of group wave fronts at the two instants, we shall now look at the phase wave fronts at the same instants. Since the measurement of phase delay time can be done much more accurately than that of group delay time, we should be able to obtain a more precise picture of wave fronts for phase. The phase wave fronts shown in Figs. 18 and 19 correspond to the peak of ground displacement with period of 200 sec in the counterclockwise direction as seen from the epicentre. The phase velocity of 4.901 km/sec is assumed in the extrapolations. The extrapolated points at 8900 sec obtained from the $G2$ data form a remarkably coherent wave front. They are nearly point-symmetric with
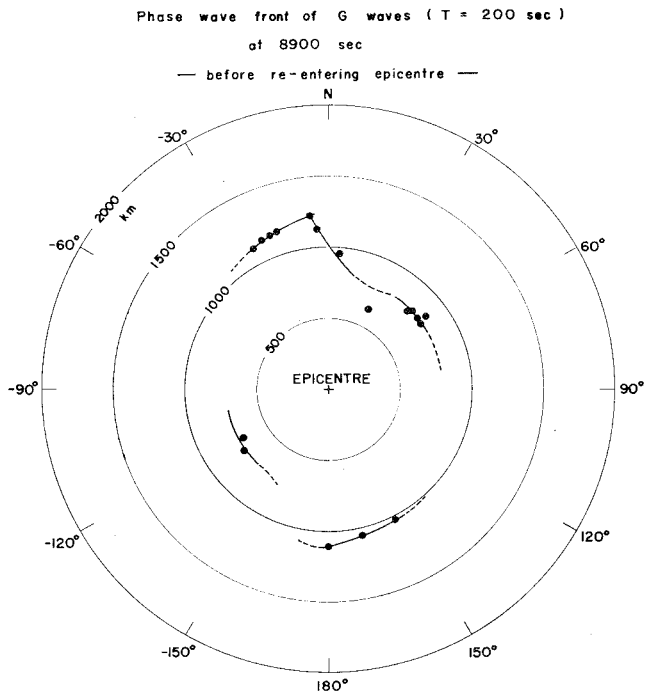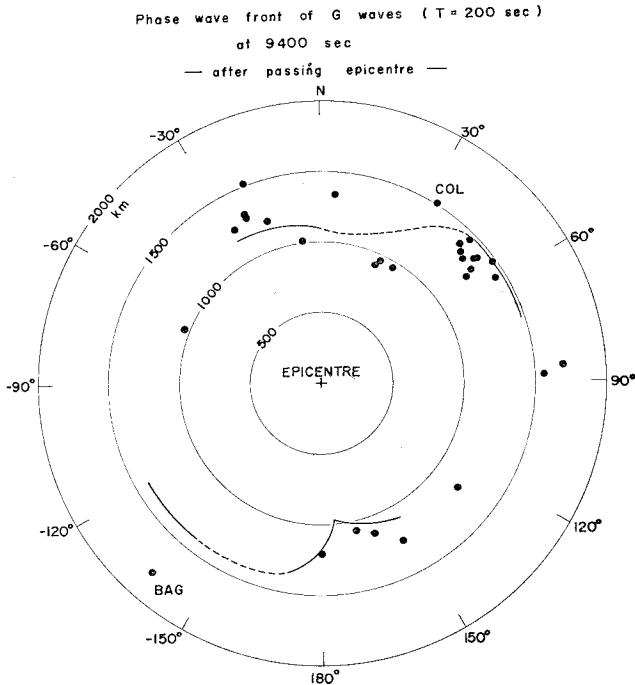
Fig. 18   The phase wave front of *G* waves with period of 200 sec at 8900 sec after the origin time as extrapolated from *G*2 data.

respect to the epicentre, and the waves in the NE–SW directions arrived about one half wave length ahead of (or behind) those in the NW–SE directions. This picture is a more realistic demonstration of the quadrantal variation of initial phase with azimuth shown in Fig. 3. The smoothed wave front at 8900 sec is advanced for additional 500 sec under the assumption that the waves proceed with the velocity of 4.901 km/sec along the great circle passing the epicentre, undergoing the $\pi/2$ polar phase advance. It is also taken into account that the direction of motion as seen from the epicentre changes its sense on crossing the epicentre. The predicted wave front is compared in Fig. 19 with the observed points obtained from the *G*3 data. The observed points scatter around the predicted wave front, lying ahead of the predicted in one azimuth and behind it in another, and show that the assumed $\pi/2$ phase advance is at least a good first approximation. The point for *COL* and *BAG*, which showed anomalous group arrivals again deviate significantly from the predicted. The remarkable coherency of the wave front before entering

Fig. 19 The phase wave front of *G* waves with period of
200 sec at 9400 sec after the origin time as extrapolated from
*G*3 data. The curve shows the extrapolation of the smooth
curve shown in Fig. 18 on the assumption of $\pi/2$ polar phase
advance.

the epicentre is lost in the "after" picture. We cannot attribute this
to poor extrapolation, because the extrapolated distances are nearly the
same for *G*2 and *G*3. We must, therefore, attribute this to a complex
interference among the waves arriving from different azimuth at the
epicentral area.

§ 9. Determination of phase velocity over a complete great circle.

The lost coherency of wave front upon a polar passage, described in
§ 8, throws some doubt on the significance of the usual method of phase
velocity determination over complete great circles. In this section, we
shall examine this problem by using data at 9 stations where G_n and
G_{n+2} waves are well recorded. The velocity is obtained by the usual
procedure from the difference of phase delay time (given in Table 3)
between the pair, corrected for the two polar passages and for appropriate

Table 13. Phase velocities over several great circles in km/sec

Station	Wave pair	Azimuth at epicentre	$f=.005$ c/s $T=200$ sec	.0065 153.8	.0080 125.0	.0095 105.3	.0110 90.9
HNR	G_4-G_2	153.4°	4.939	4.793	4.717	4.667	4.632
PTO	G_4-G_2	156.2	4.927	4.801	4.733	—	—
VAL	G_4-G_2	161.7	4.922	4.792	4.718	4.659	
KTG	G_4-G_2	173.4	4.920	4.775	4.696	4.640	4.602
GDH	G_4-G_2	4.7	4.955	4.811	4.734	4.693	4.673
TRN	G_4-G_2	25.7	4.924	4.806	4.730	4.674	4.632
COL	G_5-G_3	32.7	4.893	4.762	4.676	4.621	4.592
BAG	G_5-G_3	41.9	4.941	4.803	4.731	4.683	4.636
NHA	G_4-G_2	53.8	4.915	4.769	4.699	4.639	4.605
Average			4.926	4.790	4.715	4.660	4.625

Table 14. Portions of great circle paths in oceans and continents

Station	Azimuth at epicentre	Oceans						Continents							Ratio ocean/total	Shield
		Pacific	Atlantic	Indian	Arctic	others	total	North America	South America	Eurasia	Australia	Antarctic	others	total		
		deg.	deg.	deg.	deg.	deg.	deg.	deg.	deg.	deg.	deg.	deg.	deg.	deg.		deg.
HNR	153.4°	144	81	0	0	5	230	0	0	114	0	0	16	130	0.64	35
PTO	156.2	143	106	0	0	5	254	0	0	88	0	3	15	106	0.71	10
VAL	161.7	120	113	0	0	10	243	0	0	80	0	31	6	117	0.68	0
KTG	173.4	59	120	0	20	5	204	0	12	40	43	40	21	156	0.57	52
GDH	4.7	64	115	0	16	5	200	0	26	40	35	40	19	160	0.56	95
TRN	25.7	37	86	63	0	0	186	59	45	28	5	12	25	174	0.52	102
COL	32.7	35	63	80	0	0	178	66	46	30	0	0	40	182	0.49	75
BAG	41.9	38	70	82	0	0	190	59	49	5	0	0	57	170	0.53	40
NHA	53.8	96	47	88	0	0	231	40	44	5	0	0	40	129	0.64	13

integer multiples of period. The great circle distance is computed by the Rudoe's formula (Table 1). The result is listed in Table 13 in the order of azimuth of great circle direction at the epicentre.

The velocity varies irregularily with the azimuth of great circle direction, the difference between the highest and lowest being 1.3% of the average. In order to find if any relation exists between the velocity and the nature of great circle path, we measured the portions of the path lying in oceans and continents as listed in Table 14. The water depth of 2000 m is taken as the ocean-continent boundary. A plot of the velocity at period of 200 sec against the ratio of the oceanic path to the total in Fig. 20 demonstrates that there is no significant correlation be-
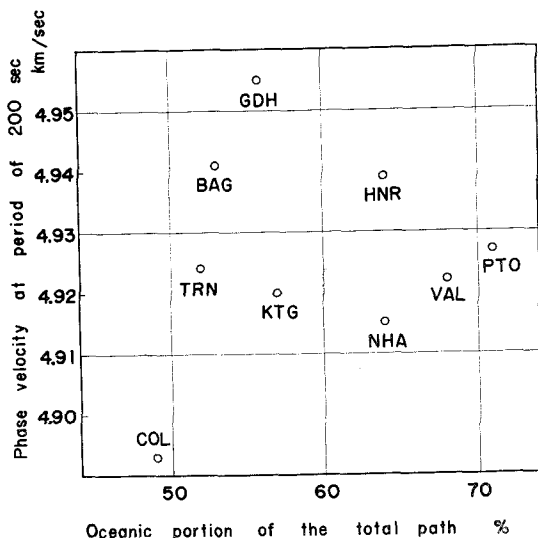
Fig. 20   The phase velocities of G waves with period of 200 sec for various great circle paths are plotted against the proportion of oceans in the total path.

tween them. Recently, Dr. D. L. Anderson of the California Institute of Technology suggested to the writer that not only the continent-ocean proportion but also the proportion of stable shield relative to a tectonically active mountain region within the continents are the important factors influencing the great circle velocities. His result[40] indicates that G wave velocity at long periods is the highest in the shield area, medium in the

40)   D. L. ANDERSON, personal communication.

ocean and lowest in the tectonically active area. A comparison[41],[42] of the G wave velocity at shorter periods between Japan and the Canadian shield also shows about 5% lower velocity for Japan.

To look at our present data from Anderson's point, we measured the portion of the great circle path within the stable shield area (Table 14), by consulting the map[43] of active mountains since the Cambrian period and the map of seismically stable masses.[44] We found that the G wave velocities at 200 sec along four great circles which satisfy the inequality

$$1.44 \times oceanic \ path \ (\text{deg.}) + shield \ path \ (\text{deg.}) > 360° ,$$

are all greater than 4.923, while those along the other five great circles which do not satisfy the above inequality are smaller than 4.923 except for the station BAG. Excluding BAG, we calculated the t value for the velocity difference between the two groups of great circles according to Eq. 8. The value is 2.303 which does not exceed the limit $t_6(0.05) = 2.447$ at the 5% level, but exceeds the limit $t_5(0.10) = 1.943$ at the 10% level. In other words, the higher velocity for great circles satisfying the above inequality is significant at the 10% level, if we exclude the station BAG. The inequality implies that increase in the oceanic path contributes more to increase in the great circle velocity than in the shield path. Our data, however, are not good enough for drawing a definite conclusion on the velocity difference between the two paths.

One interesting feature in Fig. 20 is a tendency for the scatter of observed velocities to decrease with increasing proportion of the oceanic path. This suggests that the greater the continental portion, the more complex becomes the path. In order to examine the reality of this tendency, we devided the stations into two groups, one with the oceanic proportion greater than 0.6, and the other smaller than 0.6. The ratio of the estimates of variance, the F value, is computed as 5.484, which does not exceed the limit $F_3^4(0.05) = 9.117$ on the significance level of 5%, but exceeds the limit $F_3^4(0.10) = 5.343$ on the 10% level. Thus, the above tendency is significant on the 10% level.

For estimating the accuracy of phase velocity determination along

41) J. N. BRUNE and J. DORMAN, *Bull. Seis. Soc. Amer.*, **53** (1963), 167-210.

42) K. KAMINUMA, read at the meeting of the Seismological Society of Japan, Oct., 1965.

43) J. H. F. UMBGROVE, *The Pulse of the Earth* (The Hague, Martnus Nijhoff, 1947), plate 5.

44) B. GUTENBERG and C. F. RICHTER, *Seismicity of the Earth* (Princeton Univ. Press, 1954), p. 92.

great circles, we shall look at the velocity as a function of period and great circle path, and apply the method of "analysis of variance" to the 7×5 matrix listed in Table 13 (stations PTO and VAL are excluded, because reliable measurement of velocity is not possible at short periods).

We assume that the matrix element y_{ij} $(i=1, \cdots r, j=1, \cdots s)$ obeys the Gaussian distribution with the mean value of $m+R_i+C_j$ and the variance σ^2. R_i represents the effect of path, C_j the effect of period, and for both $\varSigma R_i=\varSigma C_j=0$. We shall form the following square sums;

$$
\left.
\begin{aligned}
S_R &= \varSigma_{ij} (\overline{y_{i.}} - \overline{y})^2 , \\
S_C &= \varSigma_{ij} (\overline{y}_{.j} - \overline{y})^2 , \\
S_E &= \varSigma_{ij} (y_{ij} - \overline{y_{i.}} - \overline{y_{.j}} + \overline{y})^2 , \\
S &= \varSigma_{ij} (y_{ij} - \overline{y})^2 = S_R + S_C + S_E
\end{aligned}
\right\}
\tag{25}
$$

where

$$
\left.
\begin{aligned}
\overline{y}_{i.} &= \frac{1}{s} \varSigma_j y_{ij} , \\
\overline{y}_{.j} &= \frac{1}{r} \varSigma_i y_{ij} , \\
\overline{y} &= \frac{1}{rs} \varSigma_{ij} y_{ij} ,
\end{aligned}
\right\}
\tag{26}
$$

Then, if $R_i=0$, that is, if there is no effect of path, $F=\dfrac{(s-1)S_R}{S_E}$ will obey the F distribution with $r-1$, $(r-1)(s-1)$ degrees of freedom. If $C_i=0$, that is, if there is no effect of period, $\dfrac{(r-1)S_C}{S_E}$ will obey the F distribution with $s-1$, $(r-1)(s-1)$ degrees of freedom.

In any case, the unbiased estimate of σ^2, that is the variance of individual velocity measurement, may be obtained as $S_E/(r-1)(s-1)$.

From our data, we obtain

$$
\begin{aligned}
S_R &= 0.01385 , \\
S_C &= 0.41475 , \\
S_E &= 0.00853 , \\
\frac{(s-1)S_R}{S_E} &= 6.496 > F_{24}^4(0.05) = 2.776 ,
\end{aligned}
$$

$$\frac{(r-1)S_o}{S_E}=291.7>F^6_{24}(0.05)=2.508 ,$$

$$\frac{S_E}{(r-1)(s-1)}=0.0003554 ,$$

where $r=7$, $s=5$.

Both S_R and S_o have values greater than the limits corresponding to the 5% significance level. Thus, not only the period but also the nature of great circle path significantly influence the observed velocity. However, as shown before, the path effect is not very simple, but is a complex one which probably involves interference phenomena discussed in the preceding sections.

The standard error σ of the individual velocity measurement is estimated from S_E as 0.0189 km/sec, which is about 0.4% of the average velocity.

§ 10. Revision of the source phase of *G2* waves with period of 200 sec.

In the propagation correction for obtaining the source phase ϕ_s in § 3, we used the mean phase velocity obtained by Toksöz and Anderson. Their velocity (Table 4) is about 0.4% lower than the mean velocity obtained from great circles passing the Niigata earthquake epicentre (Table 13). If we use our mean velocity, we must subtract about 0.14 cycle from the value of ϕ_s for period of 200 sec. This revision will make the agreement between theory and observation as shown in Fig. 3 poorer. If we take into account, however, the effect of finiteness of the source, we can make the agreement as good as that shown in Fig. 3. As will be shown in Part 2 of this paper, we adopt a model of symmetric bilateral fault with total length of 100 km and repture velocity of 1.5 km/sec in interpreting the observed amplitude spectral density. For such a propagating fault, we expect a phase delay of the following amount,

$$\phi_f=\tan^{-1}\left\{\frac{\dfrac{\sin^2 X}{X}+\dfrac{\sin^2 Y}{Y}}{\dfrac{\sin X \cos X}{X}+\dfrac{\sin Y \cos Y}{Y}}\right\} ,$$

where

$$X = \frac{\omega L}{4} \left(\frac{1}{v} - \frac{\cos\theta}{c} \right),$$

$$Y = \frac{\omega L}{4} \left(\frac{1}{v} + \frac{\cos\theta}{c} \right),$$

θ is the azimuth to station measured from the fault strike, c the phase velocity, v the repture velocity and L is the total length of the fault. The phase delay ϕ_f must be added to the source phase ϕ_s shown in Fig. 3 and Eq. 6 for a finiteness correction.

For $v = 1.5$ km/sec and $L = 100$ km, the value of ϕ_s at period of 200 sec varies only from 0.081 to 0.083 cycle for any azimuth θ. The value is nearly proportional to L and inversely proportional to v. Thus, if we take the rupture velocity smaller than about 1.5 km/sec, we must add about 0.1 cycle to the source phase shown in Fig. 3. This finiteness correction compensates the correction for revised phase velocity and coincidence of the theoretical prediction to the observed will be as good as that shown in Fig. 3.

§11. Determination of Q value.

We shall determine the Q value by the use of mean amplitude spectral densities of $G2$ and $G3$ waves obtained in §6.

The mean amplitude spectral density is shown in Tables 10 and 11 for $G2$ and $G3$ waves in the loop direction (Groups 3 and 7) and node direction Groups 4 and 8. The values for $G2$ are equalized to the lapse time of 7000 sec, and those for $G3$ to the lapse time of 11000 sec, both to the epicentral distance of $90°$. Q of 120 was used in this equalization for all the periods. As mentioned before (Table 6), the equalization factor for dissipation is very close to unity and the equalized values do not depend much on the choice of Q value.

The Q values are obtained from the ratio of the equalized amplitude spectral density of $G2$ to that of $G3$ by equating it to $\exp\{(\pi \times 4000 \text{ sec})/QT\}$. The error of determination is estimated by the upper and lower limits of Q value corresponding approximately to the limits of standard errors of the mean spectral densities. The results are shown in Table 15 and Fig. 21.

The difference of Q value between the two directions is negligible at the periods of 200 sec and 90 sec. In between these periods, the node direction shows greater Q values than the loop. Since the uncertainity is great for the former, this difference is probably insignificant.

Table 15. Q values of G waves with the limits of standard error

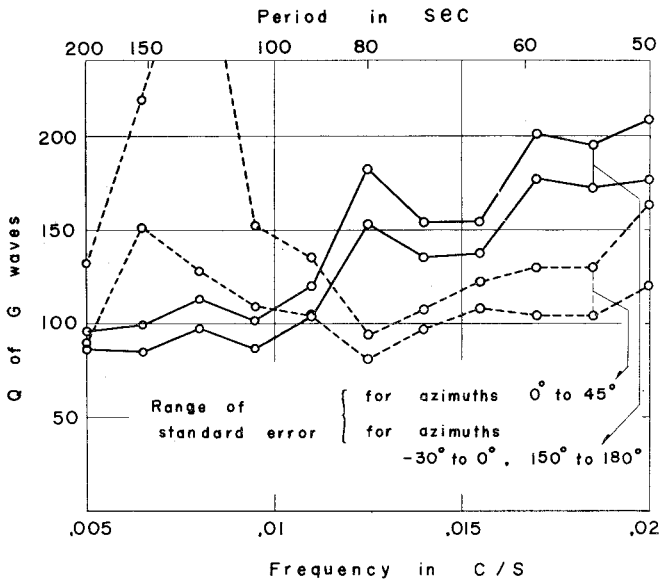| Azimuthal range		$-30°$ to $0°$, $150°$ to $180°$				$0°$ to $45°$			
freq. (c/s)	period (sec)	$G2/G3$	Q	$\underline{Q}$	$\overline{Q}$	$G2/G3$	Q	$\underline{Q}$	$\overline{Q}$
.005	200	1.99	91	86	96	1.75	112	90	132
.0065	154	2.42	92	85	99	1.55	186	151	219
.0080	125	2.61	105	97	113	1.54	233	126	322
.0095	105	3.52	95	87	102	2.47	132	109	152
.0110	91	3.45	112	104	120	3.15	121	104	135
.0125	80	2.55	168	153	182	5.93	88	81	94
.0140	71	3.36	145	135	154	5.52	103	97	108
.0155	65	3.80	146	138	154	5.42	115	108	122
.0170	59	3.09	189	177	201	6.11	118	104	130
.0185	54	3.55	184	172	195	7.26	118	104	130
.0200	50	3.56	198	186	209	5.71	144	120	163

Fig. 21 Q value determined from mean amplitude spectral densities of equalized $G2$ and $G3$ waves. The range of standard error is shown for the two azimuthal ranges; solid lines for the loop direction ($-30°$ to $0°$, and $150°$ to $180°$), dashed lines for the node direction ($0°$ to $45°$).

For shorter periods than 90 sec, the node direction shows smaller Q value than the loop, for which there is a sudden increase of Q at about 90 sec. We hesitate, however, to attribute this difference to the real difference of dissipation characteristics of crust-mantle structure, because we are not sure that the effect of constructive and destructive interferences is eliminated from the mean spectra to that accuracy. We must be satisfied, for the present, by stating that the apparent Q value of G waves can vary from 100 to 200 for periods from 200 to 50 sec.

Acknowledgement.

---

3. 1964年6月16日新潟地震によるG波の発生と伝播

(1) 統 計 的 研 究

地震研究所　安　芸　敬　一

要　　　　旨

　新潟地震によるG波の世界標準地震計の記録を用いて，発震機構をしらべた.
　周期200秒のG2波の振幅位相スペクトルの分布は，N20°E の走行をもつ逆断層で説明できる. この結果はP波初動の分布や，各種方法による震源地調査の結果とよく一致する.
　200秒より短かい波は，振幅も位相もばらつきが激しいので統計的方法で調べた. G2 も G3 も，150秒より短かい周期では，有限長のなめらかにされたガウス雑音と同じ統計的性質をもつ. このように，でたらめな波になつた理由として，(1) 震源の複雑さ，(2) 地表面に沿つて進むときの屈折に伴う干渉，(3) 高次モードの表面波や実体波との干渉などが考えられよう.
　G2 の波面を震源ちかくまで延長したものと，G3 の波面を震源ちかくまで戻したものとを比較して，極における波の伝播をしらべた. 一様な球に期待される π/2 の位相のすすみが，実際の地球でも第一近似として見られるが，G3 を戻した波面は，G2 を延長した波面よりはるかに複雑である. これは極における複雑な干渉を示していると思う. 少くとも，G3 をつかつて発震機構を論ずることは難しい.
　ある限られた方位の範囲にある観測点の振幅スペクトルを平均し，それから減衰のQ値を求めた. 周期200秒から50秒の範囲でQは大体100乃至200の間にある.